

OMAR HARIB, AYONGA HEREID,
AYUSH AGRAWAL, THOMAS GURRIET,
SYLVAIN FINET, GUILHEM BOERIS,
ALEXIS DUBURCQ, M. EVA MUNGAI,
MATTHIEU MASSELIN, AARON D. AMES,
KOUSHIL SREENATH, and JESSY W. GRIZZLE



Feedback Control of an Exoskeleton for Paraplegics

TOWARD ROBUSTLY STABLE, HANDS-FREE DYNAMIC WALKING

“I will never forget the emotion of my first steps [...]” were the words of Françoise, the first user during initial trials of the exoskeleton ATALANTE [1]. “I am tall again!” were the words of Sandy (the fourth user) after standing up in the exoskeleton. During these early tests, complete paraplegic patients dynamically walked up to 10 m without crutches or other assistance using a feedback control method originally invented for bipedal robots. As discussed in “Summary,” this article describes the hardware (shown in Figure 1) that was designed to achieve hands-free dynamic walking, the control laws that were deployed (and those being developed) to provide enhanced mobility and robustness, and preliminary test results. In this article, dynamic walking refers to a motion that is orbitally stable as opposed to statically stable.

Digital Object Identifier 10.1109/MCS.2018.2866604
Date of publication: 13 November 2018

Summary

This article presents control of a high-degree-of-freedom, fully actuated lower-limb exoskeleton for paraplegic individuals. The key novelty is the ability for the user to walk without the use of crutches or other external means of stabilization. We harness the power of modern optimization techniques and supervised machine learning to develop a smooth feedback control policy that provides robust velocity regulation and perturbation rejection. Preliminary evaluation of the stability and robustness of the proposed approach is demonstrated through the Gazebo simulation environment. Additionally, preliminary experimental results with (complete) paraplegic individuals are included for the previous version of the controller.



FIGURE 1 The ATALANTE exoskeleton designed by Wandercraft for people with paraplegia.

Approximately 4.7 million people in the United States would benefit from an active lower-limb exoskeleton to assist with overcoming the effects of stroke, polio, multiple sclerosis, spinal cord injury (SCI), and cerebral palsy [2]. By 2050, an estimated 1.5 million people in the United States will be living with a major lower-limb amputation [3]. These individuals expend up to twice the metabolic effort to walk at half the speed of able-bodied persons, experience a higher risk of falls, and have secondary pathological conditions such as osteoarthritis, back pain, and depression [4]–[6]. Lower-limb exoskeletons serve as assistive devices by providing support and balance to wheelchair users and enabling them to perform normal ambulatory functions such as standing, walking, and climbing stairs. Lower-limb exoskeletons have also been used for gait training and rehabilitation.

More importantly, standing and walking with these assistive devices provide exceptional health benefits. For paraplegics, the benefits include improved blood circulation and respiratory, urinary, and intestinal functions as well as positive psychological effects [7], which fundamentally improve their quality of life. For SCI patients, the benefits include improved bone density, cardiorespiratory function, gastrointestinal function, and sitting balance and decreased pain and spasticity [8].

The objective of this work is to translate formal control design methodologies from bipedal robots to exoskeleton systems to achieve dynamic hands-free walking. This is a formidable problem as control of biomechatronic exoskeleton devices not only shares many of the challenges of bipedal robot locomotion but also challenges introduced by the integration of an active human user. These challenges include nonlinear, high degree-of-freedom (DOF) hybrid dynamics, workspace limitations, actuator constraints, unilateral ground contact forces, robustness to variations in the user's dynamical parameters (such as mass and inertia), ability to handle interaction forces between the user and device and enforcing safety-critical constraints for the operation of the exoskeleton.

Several research groups and companies have begun responding to the need for and the benefits of exoskeletons, which can be designed for human performance augmentation and as orthotic devices. Exoskeletons for human performance augmentation enhance the strength and physical capabilities of able-bodied users; provide fatigue relief to and protection for factory and construction workers, soldiers, and disaster relief workers; and assist with carrying heavy loads for prolonged periods of time. In contrast, orthotic devices assist and restore autonomy to individuals with physical impairments that cause difficulty in walking. Orthotic devices are also designed for rehabilitation purposes, to provide gait training and therapy. A comprehensive review of current lower-limb exoskeletons can be found in [9]–[11]. See “The Cybathlon” for an example of modern exoskeletons developed for patients with disabilities.

The Cybathlon

In October of 2016, ETH Zurich hosted a one-of-a-kind race for people with disabilities using advanced assistive devices (Figure S1). The goal of the event was to enhance public awareness about the challenges faced by people with disabilities. The event also served as a common platform for technical exchange among various research organizations and companies that develop assistive biomechatronic devices for people with disabilities. A total of 66 pilots, 56 teams, 25 nations, and 400 team members participated in various races across six different disciplines, including powered arm and leg prosthesis, brain-computer interface, and powered wheelchairs and exoskeletons [S1].

The powered exoskeleton race was intended for participants with complete thoracic or lumbar spinal cord injuries. Pilots equipped with exoskeletons were asked to complete as many tasks as possible in a 10-min timeframe. These tasks were representative of common daily activities such as sitting on and standing up from a chair, walking around obstacles (slalom course), walking over ramps, navigating through doorways, and walking across tilted paths and over discrete footholds (stepping stones). The race saw participation from nine different teams. The German team (ReWalk) won first place, followed by The Institute for Human and Machine Cognition from the United States, and SG Mechatronics from the Republic of Korea. The next Cybathlon is scheduled for May 2020.

REFERENCES

- [S1] R. Riener and L. J. Seward. "Cybathlon 2016," in *Proc. IEEE Int. Conf. Systems, Man, and Cybernetics (SMC)*, 2014, pp. 2792–2794.
- [S2] ETH Zurich. Accessed on: Apr. 11, 2018. [Online]. Available: <http://www.cybathlon.ethz.ch/publications/photo-gallery.html>

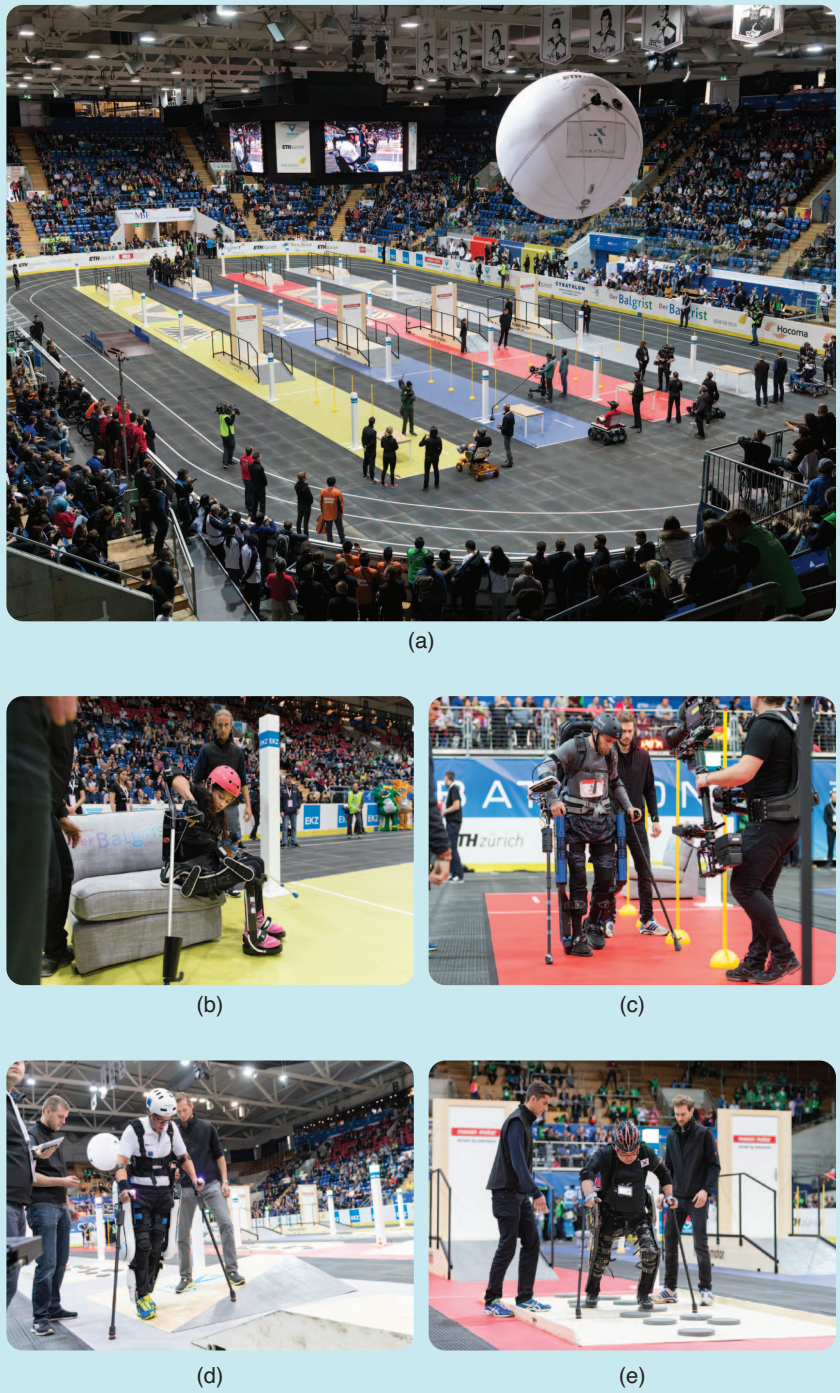


FIGURE S1 The Exoskeleton Race at Cybathlon 2016. (a) The exoskeleton race arena at Cybathlon 2016; (b) the sofa task; (c) the slalom course; (d) walking across tilted paths, and (e) the stepping stones task [S2]. [Photos (a) and (c)–(e) courtesy of ETH Zurich/Alessandro Della Bella, photo (b) courtesy of ETH Zurich/Nicola Pitaro.]

Lower-limb exoskeletons serve as assistive devices by providing support and balance to wheelchair users and enabling them to perform normal ambulatory functions such as standing, walking, and climbing stairs.

Early exoskeletons developed by General Electric [12], the University of Wisconsin [13], and the Mihailo Pupin Institute [14], [15] have focused on human augmentation or assistance, supporting multitask capabilities such as walking, standing up from a seated position, sitting down, stepping over obstacles, and climbing stairs. These capabilities are accomplished through preprogrammed motion patterns that were executed at the user's command. These systems, however, were not very robust. More recently, Ekso Bionics' robotic exoskeleton EksoGT [16] was primarily designed for use in clinical settings for rehabilitation and gait training for stroke and SCI patients. ReWalk [17], [18] is another robotic lower-limb exoskeleton that enables patients with SCI to stand up, walk, turn, and climb stairs. The hybrid assistive limb [19] developed at the University of Tsukuba, Japan, and Cyberdyne [20] provides locomotion assistance to physically challenged persons. These are high-DOF exoskeletons that have multiple actuators at the hip, knee, and ankle. A primary limitation of these exoskeletons, however, is that they require external support mechanisms such as crutches or canes for the user to maintain balance while walking. While REX Bionics' lower-limb exoskeleton provides hands-free functionality, it only allows slow static gaits with velocities of roughly 0.05 m/s.

While modern-day hardware for exoskeletons and prosthetics is becoming lighter, stronger, and power dense, the current approaches to the control of powered leg devices are rudimentary and driven by finite-state machines with several phases such as swing, stance, heel-strike, and toe-off [21], [22]. Each of these approaches contains numerous tunable parameters that are specific to each user [23], [24] (offering no formal guarantees of either stability or safety [25]) and typically require the use of additional aids such as crutches to be used safely [26], [27]. A general review of various control strategies for lower-limb assistive robotics is presented in [21], [28], and [29]. Specifically, low-level control strategies are either position based [30]–[34] or torque/force based [35]–[39], while a higher-level impedance or admittance controller is used to regulate human-device interaction forces. This is in stark contrast to the surge in control technology for highly dynamic bipedal locomotion [40]–[45], in which tools are being developed that allow for the rapid design of gaits and model-based feedback controllers that respect the physical constraints of the system (such as torque limits and joint speeds), while providing formal guarantees of stability, safety, and robustness to

uncertainties in the model and environment [46]–[50]. If the control and design methodologies underlying advanced locomotion strategies for bipedal robots can be successfully translated to powered prostheses and exoskeletons in a holistic and formal manner, then the end result promises to be a new generation of wearable robotic devices that deliver the next level of stable, safe, and efficient mobility.

A new paradigm of control design is thus necessary to achieve dynamic hands-free exoskeleton walking, one that transcends current approaches involving state machines and extensive gain tuning [51]–[54]. The heart of our approach involves virtual constraints and hybrid invariant manifolds. Virtual constraints are functional relations achieved on the generalized coordinates of the exoskeleton via feedback control; they provide a systematic means for coordinating limb motion and providing corrective actions to attenuate disturbances without resorting to low-dimensional pendulum models. The virtual constraints are designed herein on the basis of the 18DOF floating-base model of the exoskeleton and offline trajectory optimization. This approach is validated both numerically and in preclinical experimental testing, the latter of which enables hands-free walking for paraplegics, with all of the control actions required for stable dynamic walking provided by an onboard controller. We also present a recent generalization of virtual constraints based on a unique combination of a fast, offline trajectory optimization and machine learning, in tandem with robust online trajectory tracking. These newer techniques harness the power of modern optimization tools and are blazing the way for improved controller designs that deliver multiple walking speeds, turning, and enhanced robustness for exoskeleton locomotion.

In the remainder of the article, we introduce the exoskeleton mechanism under study, construct a dynamic model for control design, and develop control objectives for achieving hands-free dynamic walking. Following this, state-of-the-art techniques in bipedal control are summarized, and how to translate a method based on virtual constraints to exoskeletons is highlighted. A generalization of virtual constraints is presented that combines offline trajectory optimization and machine learning to design stabilized gaits that can be robustly tracked online. Preliminary robustness and stability analyses of both control design approaches are numerically illustrated in simulation, while preclinical tests are currently available only for the first method. In these early tests (aimed at evaluating the viability of the hardware and approaches to control

design discussed in the current article), fully paraplegic patients are able to dynamically walk hands free. Note that these tests are not aimed at assessing patient outcomes.

For transparency, in terms of gain tuning, the local controllers at the joint level will be tuned based on a nominal walking motion and then left fixed. In the early stages of optimization, the constraints are adjusted to provide adequate foot clearances, given the observed tracking errors in the local joint controllers and small errors in calibration. Postoptimization, a constant bias is sometimes added to a commanded joint profile to compensate for model or tracking errors.

THE EXOSKELETON AND ITS DYNAMIC MODEL

In this section, we first provide a brief description of the hardware and sensors of the exoskeleton. We next derive a mathematical model of walking for the human-exoskeleton system, which can be represented by a hybrid control system. The model developed is used later to determine periodic walking gaits, develop feedback controllers to stabilize these gaits, and perform numerical simulations of the hybrid control system. The most basic of these generated gaits are evaluated in experiments.

Hardware Description

ATALANTE, developed by the French startup Wandercraft, is a fully actuated lower-limb exoskeleton intended

for use in medical centers for the rehabilitation of paraplegic patients. The exoskeleton consists of 12 actuated joints, as shown in Figure 2: three joints that control the spherical motion of each hip, a single joint for each knee, and two joints for the ankle rotation in the sagittal and frontal plane in each leg, respectively. Except for the ankle (where a special mechanism is mounted), each DOF is independently actuated by a brushless dc motor. The displacement and velocity of each actuated joint are measured by a digital encoder mounted on the corresponding motor by three inertial measurement units, with one attached to the torso and one on each leg above the ankles. Four three-axis force sensors attached to the bottom of each foot are used to detect ground contact. All of the electrical components of the exoskeleton are controlled by a central processing unit that runs a real-time operating system and is in charge of high-level computations.

The mechanical design of ATALANTE allows the leg length and hip width to be manually adjusted to fit to each patient's measurements. This presents a challenge from the control design perspective, in that the controller should be robust enough to handle these physical changes of the model. Because the exoskeleton is designed to fully support the user's weight, the user is securely strapped to the device from the feet up to the abdomen, as shown in Figure 2.

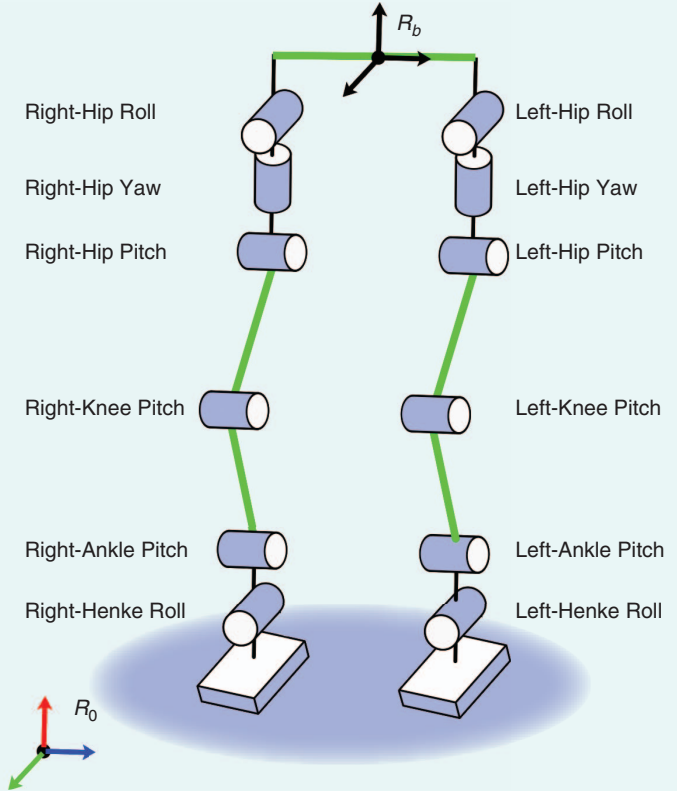


FIGURE 2 The kinematic diagram of the human-exoskeleton lumped system. The patient is secured to the exoskeleton by means of fasteners located at the ankle, shin, thigh, abdomen, and torso. The lengths of links highlighted in green are adjustable.

Pinned Versus Floating Base Models

In the “The Exoskeleton and Its Dynamic Model” section, we use a set of floating base coordinates (attached to the pelvis of the exoskeleton system) to describe the configuration of the robot’s base frame with respect to an inertial frame. The kinematic structure of the robot is then built relative to the pelvis base frame, branching into swing and stance legs.

Another approach to describe the configuration of the robot is to use a pinned open-chain kinematic model [46]. In this approach, the robot’s kinematic tree is built starting from the stance foot and branching into the torso and swing leg. It is assumed that the stance foot is attached to the ground through an ideal revolute joint. The advantage here is that the constraint forces that enforce the holonomic constraints on the stance foot no longer appear in the resulting equations of motion.

While the two models are equivalent, note that the position of the swing foot with respect to the base frame (attached to the stance foot) in the case of the pinned model involves more trigonometric (sine and cosine) terms (compared to the floating base model), where the base frame is attached to the pelvis. This is also reflected in the resulting equations of motion. One consequence is that optimizations for finding periodic orbits run faster for the floating base model compared to the pinned model.

Mathematical Representation

With the goal of studying the dynamical behavior of the human exoskeleton and avoiding overcomplication of the model by considering the compliant elements present in the human body and exoskeleton linkages, the lumped human-exoskeleton system is modeled as a rigid body system represented by a kinematic tree, as shown in Figure 2. Unlike our previous work in [53] (in which an articulated model of the human torso is considered to allow control of the exoskeleton via the user’s upper body posture), the upper body of the human in this article is modeled as a single rigid link attached to the torso of the exoskeleton. Specifically, the patient does not provide any actuation; however, the approximate masses and inertias of the patient are combined in the corresponding links of the exoskeleton. Such a model appears to be appropriate for paraplegic patients who have a complete loss of motor input in their lower extremities.

Based on the rigid-body assumption, the mathematical representation of the system dynamics can be obtained via the Euler–Lagrangian equations of motion of rigid-body dynamics. Specifically, a floating-base generalized coordinate system is considered, with the coordinate variables defined as

$$q = (p, \phi, q_b) \in Q, \quad (1)$$

where $p \in \mathbb{R}^3$ and $\phi \in SO(3)$ denote the relative position and orientation of the exoskeleton’s base frame considering the world frame, respectively, and $q_b \in \mathbb{R}^{12}$ denotes the relative angles of the actuated joints.

This article considers a simplified gait corresponding to flat-footed walking. Specifically, the gait consists of alternating phases of a continuous, single-support swing phase and an instantaneous, double-support impact phase. The stance foot is maintained flat on the ground at all times (that is, the stance foot is not allowed to roll or slip), and the swing foot is parallel to the ground at foot strike and foot liftoff. As is common practice in the control design of legged robots [55], [56], the ground contact with the stance foot is considered noncompliant. Under this assumption, the ground contact can be modeled as a holonomic constraint, which enforces the position and orientation of the stance foot to remain constant throughout the swing phase. The dynamical equations of the swing phase with stance foot contact can be obtained as

$$D(q)\ddot{q} + C(q, \dot{q})\dot{q} + G(q) = Bu + J_{st}^T(q)F_{st}, \quad (2)$$

where D , C , and G are the inertia, Coriolis, and gravity matrices, respectively, which are obtained directly from the exoskeleton’s universal robot description file [57] using FROST [58], an open-source Matlab tool kit for modeling, trajectory optimization, and simulation of hybrid dynamical systems. The Jacobian J_{st} of the holonomic constraint and ground contact wrench $F_{st} \in \mathbb{R}^6$ enforce the holonomic constraint of the stance foot being flat on the ground [56].

We note that the presented model is a floating-base model. An equivalent pinned-foot model can be developed in which the stance foot wrench does not explicitly appear in the dynamic equations. “Pinned Versus Floating Base Models” presents the advantages of one over the other.

Furthermore, under the rigid ground assumption, the swing foot impact with the ground will be considered as plastic (the coefficient of restitution is zero) and instantaneous (the impact forces and moments act over an infinitesimal interval of time) impact. During an impact, the coordinate variables of the system remain unchanged. However, the generalized velocities \dot{q} undergo a discrete jump due to the instantaneous change in the generalized momentum. This is captured by a reset map Δ , which represents the relationship between the preimpact states x^- with the postimpact states x^+ . Let $x = (q, \dot{q}) \in TQ$ be the states of the system dynamics in which TQ is the tangent space of Q . The hybrid system model of the flat-footed walking of the exoskeleton can be written as

$$\Sigma: \begin{cases} \dot{x} = f(x) + g(x)u, & x \notin S, \\ x^+ = \Delta(x^-), & x \in S, \end{cases} \quad (3)$$

where S is the guard or switching surface that determines the specific condition (for example, the swing foot impacting

the ground) that triggers the discrete events and the vector fields f, g are from the continuous-time, swing-phase dynamics in (2). See [56] for a thorough discussion on obtaining dynamical models for bipedal mechanical systems.

GAIT OBJECTIVES, IMPORTANT CONSTRAINTS, AND CONTROLLER ARCHITECTURE

The embedded control system must generate comfortable, robustly stable walking gaits that respect the mechanical limits of the exoskeleton (such as joint and torque limits), initiate smooth (not jarring) foot contact with the ground, and satisfy ground contact constraints that avoid slipping. These requirements will be the main focus of this article. In our previous work [53], we provided additional features in the closed-loop system that may provide an intuitive means for the user to regulate walking speed and eventually direction.

Gait Design Objectives

The gaits designed in this article are destined for testing in a medical facility in which an engineer or therapist will provide external commands for walking speed. A wearer's directional and speed-control interface will be tested at a later stage. Gaits will be designed for walking in a straight line at speeds that vary from -0.3 to 0.3 m/s. For comparison purposes, the relaxed human walking gait is approximately 0.9 m/s.

The time duration of a step will be set to 0.7 s. Our observation is that shorter step times closer to 0.5 s are uncomfortable for the user, although they are easier to stabilize. To limit the transmission of vibrations from the exoskeleton to the user, the impact of the swing foot with the ground must be carefully regulated. Just before impact, we try to achieve near-zero forward and lateral velocities of the foot with respect to the ground, while the downward velocity of the foot is between -0.3 and -0.1 m/s. The upper bound ensures a transversal intersection of the foot with the ground (a key guard condition in the hybrid controller), while the lower bound is for user comfort.

It is desirable for the user to maintain an upright posture when using the exoskeleton to limit demands on abdominal and dorsal muscles, which may have been weakened through the prolonged use of a wheelchair. We settled on left-right swaying motions that are lower than 2° and a forward lean angle that is between 2 and 6° . For user safety, the knee angles are bounded above 5° away from straight, and the ankles are limited to $\pm 23^\circ$. Joint safety limits are imposed through a combination of hardware and software-enforced limits.

Ground Contact

The holonomic constraints for modeling the ground are taken from [56]. The key things to note are that the ground cannot pull on a foot and a "friction cone" must be respected to avoid foot slippage, namely,

$$F_z > 0 \quad (4)$$

$$F_x^2 + F_y^2 \leq \mu^2 F_z^2, \quad (5)$$

where $[F_x, F_y, F_z]$ is a vector of ground reaction forces acting on the stance foot (as shown in Figure 3), and $0 < \mu < 1$ is the coefficient of friction.

For the gaits used in this study, we will simplify the motions of the exoskeleton by imposing that the stance foot remains flat on the ground. As explained in [56], this requires moment constraints so that that foot does not roll about one of its axes. The stance width is set at 27 cm. This relatively wide stance limits rolling around the outer edge of the stance foot, which is typically harder to recover from than rolling inward on the stance foot, and also promotes lateral stability. To provide additional robustness against foot rotation, we design the gaits so that the zero-moment point (ZMP) [59] lies in the shaded areas shown in Figure 3. Although it is not exactly the same, for the purpose of this article, the ZMP can be considered the center of pressure of the forces distributed on the sole of the foot. Additionally, due to the relatively heavy battery pack mounted just behind the user's hips, the center of mass (COM) of the exoskeleton is toward the heel of the foot when the leg is straight. Designing gaits with the ZMP toward the forward section of the foot prevents the exoskeleton from rolling backward on its stance foot. In our experience, rolling forward on the foot has not been a concern.

Other Objectives

To reduce the possibility of the swing foot prematurely contacting the ground, gaits are designed with relatively large foot clearance in the middle of the step. The heel and toe are designed to be 10 and 5 cm above the ground, respectively. Larger foot clearance results in easier handling of terrain irregularities and trip recovery via foot placement. Potential downsides include greater torque requirements and

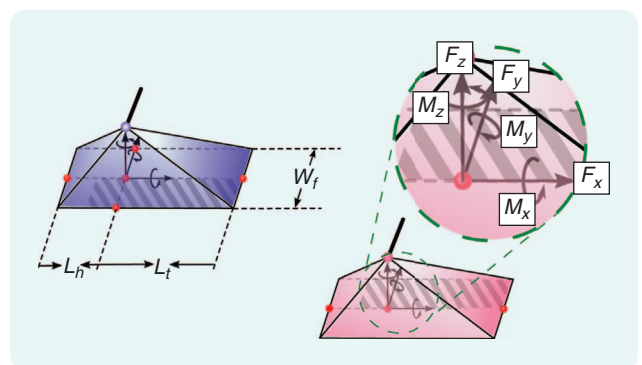


FIGURE 3 The feet of the exoskeleton, with blue representing the left foot and pink representing the right foot. L_h and L_t denote the distance from the point of reference to the heel and toe, respectively, while W_f denotes the width of the foot. The shaded area depicts the desired location of the zero-moment point. $[F_x, F_y, F_z, M_x, M_y, M_z]$ is the resultant ground reaction force and moment acting on the foot during support, respectively, described in the body coordinate of the foot.

motions that are closer to joint limits. Because flat walking is assumed, gaits must be designed such that the feet are parallel to the ground during liftoff and impact.

Controller Architecture

The overall control structure is shown in Figure 4. The control policy is responsible for specifying the evolution of key quantities of the exoskeleton, such as the torso angle, swing leg angle (a line from the hip to the ankle), and stance leg length (a line from the hip to the ankle). These synthetic quantities are often more intuitive for the control and test engineers to use when specifying and discussing gait designs.

The low-level controller is responsible for associating the synthetic high-level quantities to the individual actuators of the exoskeleton. During early testing, the simpler the low-level controller, the easier it is to make rapid changes and uncover bugs. The low-level joint controllers assure trajectory tracking with lower than 2° of error. The main task to be discussed later in this article is the association of high-level control policy objectives to individual (or pairs of) joints and motors.

As its name suggests, the guard checker monitors quantities associated with events in a gait. In the real world, leg swapping is a control decision and not a discrete, capturable event, as it would appear in an ideal simulator. The guard event for leg swapping is defined here in terms of step duration and measured vertical ground reaction force. In general, a gait-timing variable is a strictly monotonically increasing quantity that varies from zero to one over the course of a step. Here, we use $\tau = (t - t_0) / T_p$, where t_0 is the starting time of the current step and T_p is the time duration of a step. The guard for leg swapping is then

$$(GRF_{\text{swing}}^z > GRF_{\min} \text{ and } \tau > 0.5) \quad \text{or } \tau > 1, \quad (6)$$

where GRF_{swing}^z is the measured vertical component of the ground reaction force acting on the swing foot and GRF_{\min} is a chosen minimum threshold.

PARTIAL HYBRID ZERO DYNAMICS: CONTROL POLICY DESIGN ON THE BASIS OF A SINGLE PERIODIC GAIT

Given the hybrid model of the system as in (3), the first objective of this article is to design a feedback control policy that creates and robustly stabilizes a single periodic solution of the exoskeleton. Specifically, we view the combined fully actuated exoskeleton and its user as a three-dimensional bipedal mechanism. In this section, a brief description of the well-studied virtual constraints-based feedback control law for a single periodic gait is presented. In a later section, a control methodology that addresses more complex dynamical behaviors of the exoskeleton is introduced.

Virtual Constraints

At the core of this method is the design of a set of virtual constraints that modulate the joint trajectories of the system to achieve certain desired behaviors [46], [60]. Enforcing virtual constraints results in a lower-dimensional representation of the full-order system, termed the partial hybrid zero dynamics (PHZD), which captures the natural dynamics of the mechanical system. While the PHZD is a reduced-order model, it does not involve any approximations of the dynamics. Solutions of the PHZD are solutions of the original system model under feedback control.

The virtual constraints are defined as the difference between actual physical quantities and their desired evolution and then posed as outputs of the system that are to be zeroed by a feedback controller. In general, the actual outputs y^a represent important kinematic functions of the robot: they could be as simple as particular joint variables (such as the hip and knee angles), or they could also be more complicated functions of robot states (such as swing-foot orientation in the world frame or forward velocity of the pelvis). The desired outputs are often represented by a group of parameterized curves with a timing variable. In their traditional form, the virtual

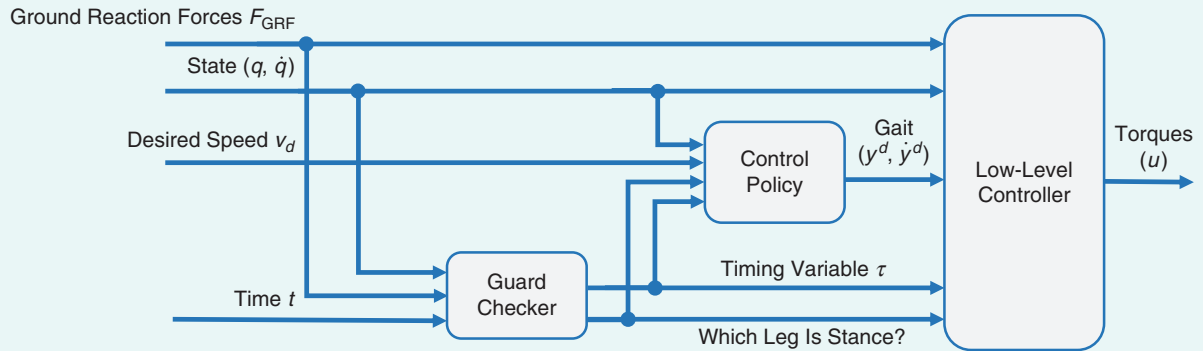


FIGURE 4 An overview of the controller structure. The guard checker detects when to swap legs. The control policy specifies the desired gait and the means to achieve it. The low-level controller translates control policy commands to the desired joint-level trajectories and achieves them via proportional-derivative control.

The advantage of studying the HZD manifold is that the evaluation of orbital stability of the full-order system can be performed on the reduced-dimensional zero dynamics.

constraints are synchronized through a state-based timing variable. Work in [61] and [62] shows that such a state-dependent design is not strictly required. To present the main idea of a virtual-constraints-based feedback control design, a state-based phase variable is still assumed in this section.

For the particular case of the human-exoskeleton system with powered ankle joints, the actual outputs are chosen to be a combination of a velocity-regulating term y_1^a and posture-modulating term y_2^a . Specifically, the velocity-regulating output is the forward hip velocity of the exoskeleton, and posture modulating outputs are chosen to represent the synchronized motion of the remaining actuated joints. Hence, the virtual constraints for the exoskeleton are defined as

$$y_1(q, \dot{q}, \alpha) = y_1^a(q, \dot{q}) - y_1^d(\alpha) \quad (7)$$

$$y_2(q, \alpha) = y_2^a(q) - y_2^d(\theta(t), \alpha), \quad (8)$$

where y_1 and y_2 are relative degree 1 and (vector) relative degree 2 by construction, and θ is a “phasing variable” [63]. To fully determine a motion of the entire system, the outputs (y_1^a, y_2^a) must be linearly independent, and their rank must be equal to the number of actuators in the system. y_1^a is set to be the forward hip velocity, while y_2^a is set to be all joint angles of the exoskeleton, except for the sagittal stance ankle [54].

Input–Output Linearization

With the goal of driving the virtual constraints in (7) and (8) to zero exponentially, the following feedback control law, based on input–output linearization, is considered:

$$u = -\mathcal{A}^{-1} \left(\begin{bmatrix} L_f y_1(q, \dot{q}, \alpha) \\ L_f^2 y_2(q, \dot{q}, \alpha) \end{bmatrix} + \begin{bmatrix} \epsilon y_1(q, \dot{q}, \alpha) \\ 2\epsilon \dot{y}_2(q, \dot{q}, \alpha) \end{bmatrix} + \begin{bmatrix} 0 \\ \epsilon^2 y_2(q, \alpha) \end{bmatrix} \right), \quad (9)$$

with a control gain $\epsilon > 0$ and decoupling matrix

$$\mathcal{A} = \begin{bmatrix} L_g y_1^a(q, \dot{q}) \\ L_g L_f y_2(q, \dot{q}, \alpha) \end{bmatrix}, \quad (10)$$

where L_f and L_g represent the Lie derivatives with respect to the vector fields $f(x)$ and $g(x)$ in (3). With a specific choice of virtual constraints, the decoupling matrix \mathcal{A} is invertible. Applying this control law to (3) yields linear output dynamics of the form

$$\dot{y}_1 = -\frac{1}{\epsilon} y_1, \quad (11)$$

$$\dot{y}_2 = -2\frac{1}{\epsilon} \dot{y}_2 - \frac{1}{\epsilon^2} y_2, \quad (12)$$

which has an exponentially stable equilibrium at the origin.

Hence, the directly actuated variables of the system are regulated to a reduced-dimensional surface called the *zero dynamics*, which is invariant within the duration of continuous swing phase, as illustrated in Figure 5(a) [46], [60]. However, due to the discrete joint velocity changes in the system’s states at swing foot impact, the controller in (9) does not necessarily guarantee that the reduced-dimensional surface is invariant through the impact. It is shown in [46] that, if there exists a set of virtual constraints such that the reduced-dimensional zero dynamics surface is invariant through impact, then the full-order dynamics of the hybrid system model restricts to a hybrid-invariant, reduced-dimensional submanifold. The restriction dynamics and invariant surface is the HZD. This requires finding a set of parameters α for the virtual constraints, such that the zero dynamics is invariant through impact maps [see Figure 5(b)]. Finding such parameters is typically formulated as a nonlinear optimization problem [50], [60]. The advantage of studying the HZD manifold is that the evaluation of orbital stability of the full-order system can be performed on the reduced-dimensional zero dynamics.

Generation of a Periodic Gait

Periodic walking gaits are periodic orbits of the corresponding hybrid system model. A solution $\varphi(t)$ of the hybrid system in (3) is *periodic* if there exists a finite $T > 0$, such that $\varphi(t+T) = \varphi(t)$ for all $t \in [t_0, \infty)$. A set $O \subset TQ$ is

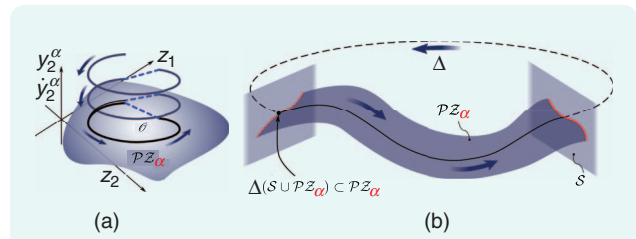


FIGURE 5 A periodic orbit on the partial hybrid zero dynamics (PHZD) surface. A PHZD surface admitting a periodic orbit is designed by selecting a proper parameter set α in the virtual constraints through optimization. (a) A periodic orbit and (b) a hybrid invariance.

a periodic orbit of the system if $O = \{\varphi(t) \mid t \geq t_0\}$ for some periodic solution $\varphi(t)$. The stability of the periodic orbit can be determined by the stability of the fixed point by evaluating the spectral radius of the Jacobian of the Poincaré map at the fixed point. More specifically, if all eigenvalues lie within the unit circle (have a magnitude lower than one), then the periodic orbit is locally exponentially stable.

To design a periodic gait for the hybrid system model of the exoskeleton, a direct collocation-based gait optimizer is used. The mathematical foundation behind the optimization technique used is briefly introduced in “How Direct Collocation Works.” Other ways of solving the optimization

can be used, such as single-shooting methods. Direct collocation, however, was found to be the fastest and most efficient way to solve this problem [50]; the stable walking gaits are obtained in minutes. Considering that our goal in this section is to find parameters for the virtual constraints instead of open-loop trajectories, we incorporate the feedback controller into the optimization in a way that is similar to holonomic constraints. Rather than enforcing the control input directly, as in (9), we impose equality constraints on system states, so that they satisfy the output dynamics in (11) and (12). Furthermore, the hybrid-invariance is enforced in the periodic gait optimization as a constraint. For a

How Direct Collocation Works

The direct collocation trajectory optimization uses the collocation methods for solving ordinary differential equations based on the finite-step implicit Runge–Kutta methods [S3]. Here, the specific formulation of the Hermite–Simpson algorithm (one of the most commonly used direct collocation schemes) is introduced. Consider a system of the form $\dot{x} = f(x, u)$. A trajectory optimization problem for this system can be stated as

$$\begin{aligned} J(x(t), u(t)) &= \min_{u(t)} \int_0^T L(x(t), u(t)) dt, \\ \text{subject to } x(t) &= \int_0^t f(x(t), u(t)) dt, \\ 0 \geq c(x(t), u(t)), \quad 0 \leq t \leq T, \end{aligned} \quad (\text{S1})$$

where $L(\cdot)$ represents the running cost function, and $c(\cdot)$ represents the path constraints. To solve this problem using direct collocation, a discrete representation of the continuous time solution is introduced. Specifically, the time interval $t \in [0, T]$ is divided into a fixed number of uniformly distributed intervals (see Figure S2). In particular, the even-numbered nodes (for example, t_0, t_2, \dots, t_N) are called cardinal nodes, and the odd-numbered nodes between every two cardinal nodes are called interior nodes. At each discrete node of $t = t_i$, an approximation of state variables $x_i = x(t_i)$ and control inputs $u_i = u(t_i)$ is introduced as a set of optimization variables to be

solved. In this article, the approximation of the slope of state variables $\dot{x}_i = \dot{x}(t_i)$ is also introduced as defect variables in the optimization.

The Hermite–Simpson methods then use piecewise continuous cubic interpolation polynomials to approximate the solution of the system over each interval between two neighboring cardinal nodes. This approximation can be fully determined by the approximated state variables and slopes at the cardinal nodes. Hence, if the approximated states x_i and slopes \dot{x}_i at the interior nodes match the interpolation polynomial at time $t = t_i$ (for example, \bar{x}_i and $\dot{\bar{x}}_i$ in Figure S2), then the resulting piecewise polynomials are considered an approximated solution of the system [S4]. To find this approximated solution (the discrete representation of the states), the original continuous time trajectory optimization problem can be converted to the following form given by

$$\begin{aligned} J(x_i, u_i) &= \min_{u_i} \sum_{i=1}^{N-1} w_i L(x_i, u_i), \\ \text{subject to } \dot{x}_i &= f(x_i, u_i) \\ c(x_i, u_i) &\geq 0, \quad 0 \leq i \leq N \\ \dot{x}_i - 3(x_{i+1} - x_{i-1})/[2\Delta t_i] + (\dot{x}_{i-1} + \dot{x}_{i+1})/4 &= 0 \\ x_i - (x_{i+1} + x_{i-1})/2 - \Delta t_i(\dot{x}_{i-1} - \dot{x}_{i+1})/8 &= 0, \end{aligned} \quad (\text{S2})$$

where, for all $i \in \{1, 3, \dots, N-1\}$ (where $\Delta t_i = t_{i+1} - t_{i-1}$ is the time interval between two cardinal nodes), w_i is the weighting factor of each node determined by the Gaussian quadrature [50]. Specifically, the last two constraints are called *collocation constraints*, which are determined by cubic interpolation polynomials. The above nonlinear programming (NLP) problem can be solved straightforwardly by existing numerical NLP solvers.

REFERENCES

- [S3] J. T. Betts, “Survey of numerical methods for trajectory optimization,” *J. Guid., Control, Dyn.*, vol. 21, no. 2, pp. 193–207, 1998. doi: 10.2514/2.4231.
- [S4] C. R. Hargraves and S. W. Paris, “Direct trajectory optimization using nonlinear programming and collocation,” *J. Guid., Control, Dyn.*, vol. 10, no. 4, pp. 338–342, 1987. doi: 10.2514/3.20223.

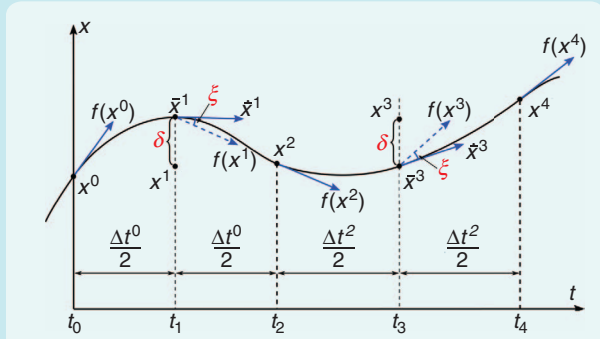


FIGURE S2 An illustration of defect constraints and node distribution of the direct collocation optimization [50].

The result of the optimization is a single periodic orbit and a feedback controller that renders it locally exponentially stable in the model of the user plus exoskeleton.

detailed setup of the optimization problem in the context of the exoskeleton, the reader is referred to [53] and [54]. Torque limits and joint position and velocity limits of the ATALANTE mechanism are directly enforced as boundary conditions on decision variables in the optimization, whereas friction cone and zero-moment constraints of foot contacts are enforced as extra physical constraints. Moreover, several constraints are considered in the optimization to narrow down the search space and address certain aspects specific to human-friendly walking. Impact velocities, ZMP position, COM position, and torso orientation are examples of the many constraints that must be considered.

The result of the optimization is a single periodic orbit and a feedback controller that renders it locally exponentially stable in the model of the user plus exoskeleton. Simulations of the controller can be found in [53]. The experiments reported later are based on the design process described above.

GENERALIZED HYBRID ZERO DYNAMICS: HARNESSING THE POWER OF MODERN OPTIMIZATION TECHNIQUES

When the HZD and PHZD methods were created, it took several hours for the computation of a single periodic orbit. At that time, it was very important to build a controller that was capable of rendering the periodic orbit locally exponentially stable directly from the orbit itself, without requiring further optimizations. The current situation is completely different, as can be seen in Table 1. How to harness this power is the overriding question.

The control loops on the exoskeleton run at 1 KHz, and the duration of a walking step is approximately 500–750 ms. Hence, online model predictive control (MPC) (that is, iteratively solving a finite horizon-constrained optimization problem in real time) is simply not possible for models with 20 or more state variables. Explicit MPC is not possible either because one would have to numerically sample the state space, complete the optimization offline, and then store the control actions for use online. A sparse uniform grid of ten samples per dimension would require 10^{20} optimizations; random sampling would provide a smaller, more effective discretization of the state space, but not enough is gained to handle $n \geq 20$.

In [64], generalized HZD (G-HZD), a new approach to control design for a class of high-dimensional nonlinear systems, is introduced. As with PHZD, the design process for G-HZD begins with trajectory optimization to design

an open-loop periodic walking motion of the high-dimensional model. It differs from PHZD in that it exploits the fact that the trajectory optimization can be done rapidly to add to this periodic solution a carefully selected set of additional open-loop trajectories of the model that steer toward the nominal motion, thereby directly building in stability. One drawback of trajectories is that they provide little information on how to respond to a disturbance. To address this shortcoming, supervised machine learning is used to extract a low-dimensional state-variable realization of the open-loop trajectories. The periodic orbit is now an attractor of the low-dimensional, state-variable model, but it is not attractive in the full-order system. The special structure of mechanical models associated with bipedal robots is used to embed the low-dimensional model in the original model in such a manner that the desired walking motions are locally exponentially stable.

In the next section, we present the main ideas underlying G-HZD for models given by ordinary differential equations. The small technical changes required to address hybrid models are discussed in [64].

Step 1: Constructing Z_0 , the Boundary of the Generalized Hybrid Zero Dynamic Surface, from a Collection of Periodic Orbits

The dynamic model of the exoskeleton is decomposed into a low-dimensional, weakly actuated portion corresponding roughly to the x - and y -coordinates and velocities of the hips (in the world frame) and a strongly actuated portion of the model that captures the hips, knees, and swing

TABLE 1 A performance comparison between direct-collocation optimization versus the classic shooting approaches on a five-link planar biped (single shooting) and a seven-link, spring-leg planar biped, respectively. CPU: central processing unit.

Method	CPU Time (s)
Single shooting (fmincon)	162.59
Direct collocation (IPOPT)	1.60
Method	CPU Time (s)
Multiple shooting (fmincon)	5027.45
Direct collocation (IPOPT)	41.47

As with PHZD, the design process for G-HZD begins with trajectory optimization to design an open-loop periodic walking motion of the high-dimensional model.

ankle joints. Specifically, the dynamic portion of the hybrid model (3) is decomposed as

$$\begin{aligned}\dot{x}_1 &= f_1(x_1, x_2, u_1) \quad x_1 \in R^{n_1} \\ \dot{x}_2 &= f_2(x_1, x_2, u_1, u_2) \quad x_2 \in R^{n_2},\end{aligned}\quad (13)$$

where x_1 represents the “weakly actuated” portion of the model, u_1 are the stance ankle torques, and x_2 captures the strongly actuated part of the model and the remaining actuators u_2 . With this decomposition, $n_1 \ll n_2$; for the exoskeleton as modeled here in single support, $n_1 = 4$ and $n_2 = 20$.

Next, a library of gaits is constructed by uniformly discretizing a bounded set of initial conditions for x_1 . Without loss of generality, each periodic gait is assumed to start from the origin, that is, the hip positions ($x; y$) are at the origin. As a consequence, the periodic gaits are parameterized by the ($x; y$) velocities of the hip, corresponding to walking forward, backward, and sideways. Turning is not presently addressed, but it will be in the near future.

A nonlinear mapping is then constructed between the x_1 and x_2 states for the periodic orbits, such that $x_2 = \gamma(x_1)$. The function γ is called an insertion map and can be constructed in several ways. One effective approach is to numerically fit a surface to the initial conditions of the periodic orbits through machine-learning tools, resulting in

$$Z_0 := \{x = (x_1; x_2) \mid x_2 = \gamma(x_1)\}, \quad (14)$$

as illustrated in Figure 6. In the ideal case, every point on the surface Z_0 corresponds to an initial condition for a periodic orbit.

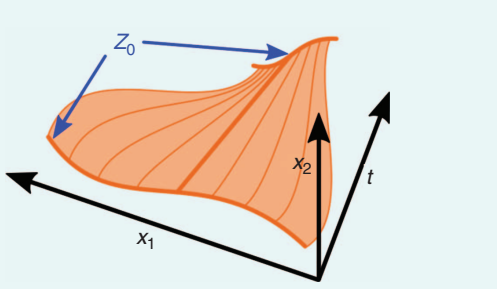


FIGURE 6 A collection of trajectories forming a smooth surface. While this is the desired outcome, it is not guaranteed. Direct collocation-based optimization is used to design the trajectories.

Step 2: Constructing Z , the Generalized Hybrid Zero Dynamic Surface

Assume now that one of the periodic orbits has been selected, corresponding to a point $\xi^* \in Z_0$. The process of stabilizing this particular periodic orbit is based on computing a judiciously selected set of open-loop trajectories of the full-order model that approach the periodic solution. Specifically, let B be an open ball about ξ^* and select a “contraction factor” $0 < c < 1$. For each initial condition $\xi \in B \cap Z_0$, a solution of the ordinary differential equation (13) with initial condition ξ is sought that satisfies the physical constraints given in the “Gait Design Objectives” section, terminates in Z_0 at time $t = T_p$, and approaches the periodic solution, as measured by $\|\varphi_\xi(T_p) - \xi^*\| \leq c \|\xi - \xi^*\|$. Transient solutions that approach periodic solutions are called *transition gaits*.

Denote the corresponding input and state trajectories parameterized by the initial condition $\xi \in B \cap Z_0$ as

$$\begin{aligned}u_\xi &: [0, T_p] \rightarrow R^m, \\ \varphi_\xi &: [0, T_p] \rightarrow R^n.\end{aligned}\quad (15)$$

If successful, the process results in a smooth surface Z of dimension equal to that of Z_0 plus one (due to time), as shown in Figure 6. As discussed in [64], these solutions may or may not exist and, in principle, could be very “ugly” functions of ξ (nonsmooth). We note that because for all $\xi \in Z_0$, $\varphi_\xi(T_p) \in Z_0$. Trajectories that start in Z_0 can be continued indefinitely.

Step 3: State-Variable Realization of the Open-Loop Trajectories Forming Z

While the above process results in complete trajectories for the model, we do not directly use these for tracking because

- 1) if the system starts on the surface Z and a perturbation occurs between $t = 0$ and $t = T_p$, it would attempt to converge back to the potentially far away original trajectory $\varphi_{xi}(t)$ until $t = T_p$, at which point only a trajectory-based controller would update the desired trajectory
- 2) if the system does not start on the surface, there is no obvious choice of a trajectory to follow.

We first address 1) by seeking a means to continuously update the desired evolution of the system to immediately respond to a perturbation. In fact, we will design a low-dimensional differential equation that evolves on the surface and has the desired periodic orbit as its locally stable

and attractive limit cycle. A solution to 2) will be given in step 5.

Figure 7 motivates a condition for “automatically replanning” to respond to a disturbance, namely,

$$x(t) = \varphi_\xi(t) \Rightarrow u(t, x(t)) = u_\xi(t). \quad (16)$$

This is an implicit interpolation condition for specifying a control response at each point of the surface Z in Figure 6. As explained further in [64], a solution to (16) can be constructed if one can find two T_p -periodic functions, ν and μ , satisfying the following conditions on the trajectory data: For all $0 \leq t < T_p$,

$$\begin{aligned} \nu(t, \pi_1 \circ \varphi_\xi(t)) &= \pi_2 \circ \varphi_\xi(t), \\ \mu(t, \pi_1 \circ \varphi_\xi(t)) &= u_\xi(t), \end{aligned} \quad (17)$$

where $\pi_i: \mathbb{R}^n \rightarrow \mathbb{R}^{n_i}$ are the canonical projections [so that $\pi_1(x_1, x_2) = x_1$ and $\pi_2(x_1, x_2) = x_2$]. Moreover, it can then be shown that 1) the trajectories of Figure 6 are solutions of the reduced-order model

$$\begin{aligned} \dot{x}_1 &= f_1(x_1, \nu(t, x_1), \mu_1(t, x_1)), \\ x_2 &= \nu(t, x_1), \end{aligned} \quad (18)$$

and 2) the periodic orbit $\varphi_{\xi^*}: [0, T_p] \rightarrow \mathbb{R}^n$ is locally exponentially stable. In fact, by construction, all initial conditions $\xi \in Z_0$ for which feasible model solutions have been found result in trajectories that converge to the periodic orbit. Hence, as one builds the feasible solutions in (15), one is constructing the domain of attraction of the periodic orbit in the G-HZD surface, Z .

Figure 8 shows the sagittal-plane hip velocity for several initial conditions in Z_0 . Two things are important to note: 1) the convergence to the nominal orbit and 2) the trajectories are feasible solutions of the full-order model. In step 4, we address how to find functions satisfying the conditions in (17).

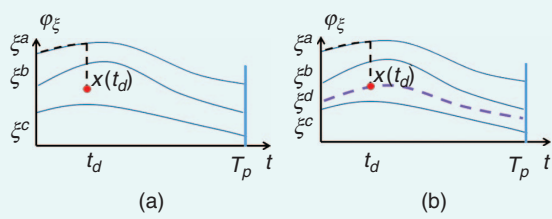


FIGURE 7 A Gedanken experiment. (a) A disturbance occurs at time t_d . Assume that the system is initialized at ξ^a , with input $u_{\xi^a}(t)$ being applied. Hence, its solution evolves along $\varphi_{\xi^a}(t)$. Suppose that, at time t_d , an “impulsive” disturbance instantaneously displaces the solution to a point $x(t_d)$. (b) The proposed “course” correction. If there exists an $\xi^d \in Z_0$ such that $x(t_d) = \varphi_{\xi^d}(t_d)$, then applying the input $u_{\xi^d}(t)$ for $t_d \leq t < T_p$ will move the system toward the equilibrium in the sense that $\|\varphi_{\xi^d}(T_p)) - \xi^*\| \leq c \|\xi^d - \xi^*\|$. This leads to interpolation, such as the learning conditions in (17).

Step 4: Supervised Machine Learning to Extract ν and μ from Optimization Data

The importance of finding a differential equation (or vector field) realization of the trajectories in Figure 6 is that the differential equation is an automatic, instantaneous replanner of the system’s evolution when it is perturbed off a nominal motion; Figure 9 shows such a realization. Solving for the functions in (17) is the key to constructing the vector field. Doing so analytically would be a challenge at best, and this is where supervised machine learning comes into play. Table 2 shows a vanilla implementation in which the features are selected as time and the x_1 states, and the labels or targets are taken as the inputs u and the x_2 states. In the control implementations simulated here, the features

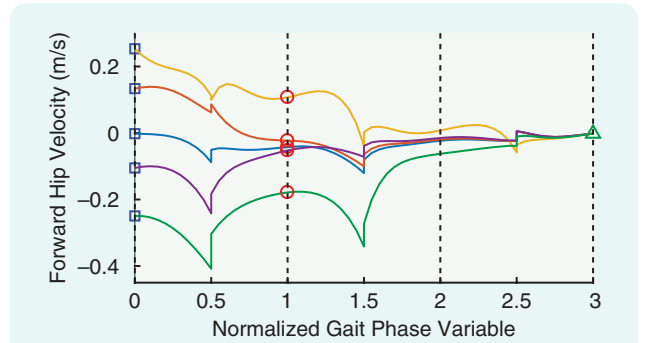


FIGURE 8 The forward velocity of the hip resulting from the transition optimizations. The black vertical-dashed lines mark the midpoint of each (robot) step in the optimization, whereas the discontinuities (jumps) in velocity between the two dashed lines arise from the rigid impact at the end of each step. The squares, circles, and triangle represent points where the state of the system is in Z_0 . The blue squares represent starting states obtained from periodic gaits, while the green triangle represents the ending desired state, also obtained from a periodic gait. The red circles were made to be in Z_0 through an optimization constraint. The gait trajectory from the blue square to the red circle is used as training data for the supervised machine learning.

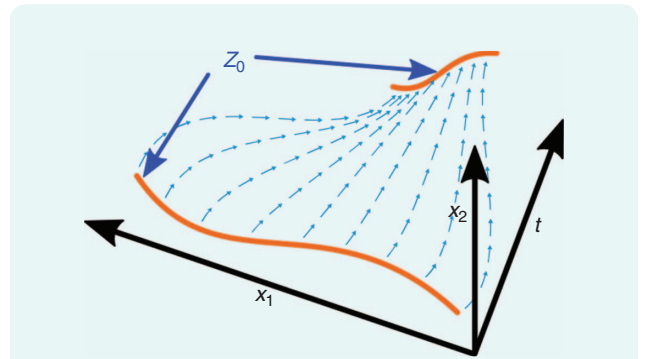


FIGURE 9 A vector field that gives rise to the trajectories is constructed, so it is a state-variable realization. Supervised machine learning and model structure are used to extract the vector field from the trajectory optimization data.

TABLE 2 A conceptual arrangement of the optimization data from which appropriate functions for building a stabilizing controller can be determined by regression. Here, ξ^i , $1 \leq i \leq M$ is a discretization of Z_0 ; t_j , $1 \leq j \leq N$ is a discretization of $[0, T_p]$; $\varphi_{\xi}(t)$ is the solution of the full model with the initial condition ξ at $t=0$; π_1 is the projection onto the x_1 -coordinate; π_2 is the projection onto the x_2 -coordinate; and $u_{\xi}(t)$ is the input giving rise to the solution $\varphi_{\xi}(t)$. Standard toolboxes in Matlab are used to build the functions and test for their existence via the quality-of-fit tools.

	Features	Labels or Targets	
t_j	$x_1^{j,i} = \pi_1 \circ \varphi_{\xi^i}(t_j)$	$v^{j,i} = \pi_2 \circ \varphi_{\xi^i}(t_j)$	$\mu^{j,i} = u_{\xi^i}(t_j)$
$t_0 = 0$	$x_1^{0,1}$	$v^{0,1}$	$\mu^{0,1}$
$t_0 = 0$	$x_1^{0,2}$	$v^{0,2}$	$\mu^{0,2}$
\vdots	\vdots	\vdots	\vdots
$t_0 = 0$	$x_1^{0,M}$	$v^{0,M}$	$\mu^{0,M}$
t_1	$x_1^{1,1}$	$v^{1,1}$	$\mu^{1,1}$
\vdots	\vdots	\vdots	\vdots
t_1	$x_1^{1,M}$	$v^{1,M}$	$\mu^{1,M}$
\vdots	\vdots	\vdots	\vdots
$t_N = T_p$	$x_1^{N,1}$	$v^{N,1}$	$\mu^{N,1}$
\vdots	\vdots	\vdots	\vdots
$t_N = T_p$	$x_1^{N,M}$	$v^{N,M}$	$\mu^{N,M}$

TABLE 3 The mapping between higher-level control objectives and their realization at a lower level.

Outputs	Actuated Joints
Torso pitch, roll, and yaw orientation	Stance hip pitch, roll, and yaw joints
Stance knee joint	Stance knee joint
Swing knee joint	Swing knee joint
Stance pitch ankle joint	Stance pitch ankle joint
Stance Henke ankle joint	Stance Henke ankle joint
Swing hip pitch joint	Swing hip pitch joint
Swing hip roll joint	Swing hip roll joint
Swing foot pitch, roll, and yaw orientation	Swing pitch and Henke ankle joints and swing hip yaw joint

are taken as the Cartesian hip velocities only (the positions are discarded), and the labels are taken as the outputs listed in Table 3.

At this point, all the functions needed to implement a control policy that locally exponentially stabilizes the selected periodic walking gait are available. Figure 10 shows

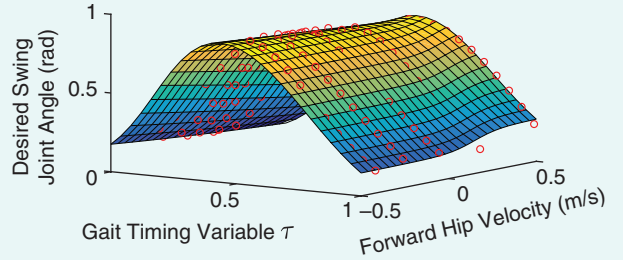


FIGURE 10 The surface showing the desired swing knee angle as a function of the gait-timing variable τ and the forward hip velocity for stabilizing the step-in-place gait. The red circles are the actual data obtained from optimization, while the surface is a regression completed using the Neural Network Toolbox in Matlab. Note that some of the circles are under the surface and, therefore, not visible.

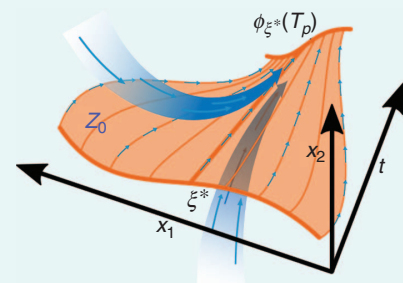


FIGURE 11 The low-dimensional realization (invariant surface and vector field) being rendered attractive in the full-order model.

one component of the function v arising from the supervised machine learning.

Step 5: Feedback Control to Render Z Attractive

The previous steps created a low-dimensional dynamical model for which the desired periodic orbit with initial condition $\xi^* \in Z_0$ is locally stable and attractive in Z . The next step is to stabilize the orbit in the full model, as illustrated in Figure 11. For this, we must be more specific about the x_2 portion of the model. In the case of the exoskeleton, the strongly actuated part of the model is fully actuated and, therefore feedback linearizable [65]. Specifically, the x_2 part of the model (13) can be expressed as

$$x_2 = \begin{bmatrix} x_{2a} \\ x_{2b} \end{bmatrix} \text{ and } f_2 = \begin{bmatrix} x_{2b} \\ \alpha(x_1, x_2) + \beta_1(x_1, x_2)u_1 + \beta_2(x_1, x_2)u_2 \end{bmatrix}, \quad (19)$$

where β_2 is square and invertible.

In [64], it is shown that for all $(n_2/2) \times (n_2/2)$ positive-definite matrices K_p and K_d , $\varphi_{\xi^*}: [0, T_p] \rightarrow \mathbb{R}^{n_2}$ is a locally uniform exponentially stable solution of the closed-loop system

$$\begin{aligned}
\dot{x}_1 &= f_1(x_1, x_2, u_1) \\
\dot{x}_2 &= f_2(x_1, x_2, u_1, u_2) \\
u_1 &= v_1 \\
u_2 &= [\beta_2(x_1, x_2)]^{-1}(-\alpha(x_1, x_2) - \beta_1(x_1, x_2)u_1 + v_2) \\
\begin{bmatrix} v_1 \\ v_2 \end{bmatrix} &= \mu(t, x_1) - [K_p \ K_d](x_2 - \nu(t, x_1)). \tag{20}
\end{aligned}$$

Step 6 (Optional): Enriching the Control Policy to Handle Multiple Gaits

The final step performed with the ATALANTE model is to repeat steps 1–5 for a grid of periodic gaits corresponding to a range of walking speeds captured in Z_0 . The trajectory designs for these new gaits are catenated to Table 2, with the only change being that the feature set is augmented to include the designed average (Cartesian) velocity of each gait. Supervised machine learning, if successful, then produces a control policy that allows a desired walking speed to be selected.

Remark on Trajectory Design via Optimization

We provide a few details on how to actually generate the trajectories in (15) that form the surface in Figure 6. We use optimization to determine solutions of the model; see “How Direct Collocation Works” for more details on the optimization method itself. In particular, a cost function of the form

$$\begin{aligned}
J(\xi) &= \min_{u_\xi} \int_0^{3T_p} L(\varphi_\xi(\tau), u_\xi(\tau)) d\tau, \\
\text{subject to } \varphi_\xi(t) &= \xi + \int_0^t f(\varphi_\xi(\tau), u_\xi(\tau)) d\tau, \\
0 &\geq c(\varphi_\xi(t), u_\xi(t)), \quad 0 \leq t \leq 3T_p \\
\varphi_\xi(T_p) &\in Z_0, \quad \|\varphi_\xi(T_p) - \xi^*\| \leq c \|\xi - \xi^*\| \\
\varphi_\xi(3T_p) &= \xi^*, \tag{21}
\end{aligned}$$

with constraints is posed over a time horizon of three steps such that

- » energy per step taken is penalized
- » solutions satisfy the full-order model
- » key constraints on ground reaction forces and actuator limits are respected (captured in the function $c \leq 0$)
- » the solution returns to Z_0 in one step so that trajectories can be continued indefinitely while approaching the desired periodic orbit
- » the nominal periodic orbit terminates in three steps (this could be replaced by a terminal penalty in the cost function).

The choice of three (robot) steps in the optimization is based on the capture-point analysis in [66] and theoretical work in [64]. $L(\varphi_\xi(\tau), u_\xi(\tau))$ defines the running cost, while $f(\varphi_\xi(\tau), u_\xi(\tau))$ are the dynamics of the system. Figure 12 shows a conceptual representation of the gait design process.

NUMERICAL ILLUSTRATION

This section presents simulation results of the G-HZD controller developed in the previous section. The simulation

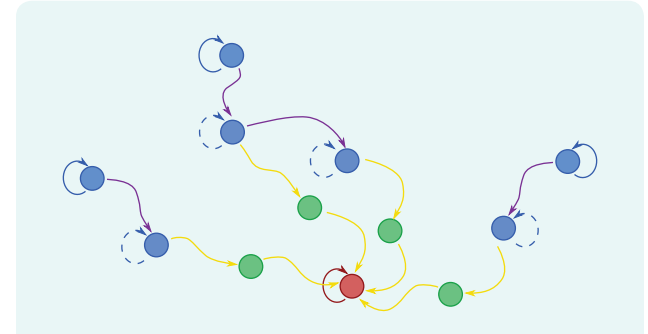


FIGURE 12 A graphical representation of gait optimization. Each arc represents one step of the exoskeleton. Circles with self-loops denote periodic orbits, while those without self-loops are transient states. The red circle denotes the goal (periodic) gait. The optimizations are completed in three steps. The end of the first step is required to terminate in Z_0 (which is parameterized by periodic gaits), and the end of the third step must be the goal state. Note that, since the first step initiates and ends in Z_0 , the three-step optimization can continue from the end of a first step and other self-loop states. The (first-step) trajectories corresponding to the time interval $[0, T_p]$ —denoted by the purple arcs—are saved and used as training data for the supervised machine learning. The other data are discarded.

experiments were conducted with Gazebo using the full dynamical model of the exoskeleton with a human in it. The ground contact model in Gazebo allows for the possibility of the feet to roll and slip. In these tests, the machine-learning approach based on G-HZD was used to stabilize walking motions with a longitudinal speed range of -0.3 to 0.3 m/s.

Velocity Tracking

Figure 13 shows a simulation in which the exoskeleton starts by stepping in place at $t = 0$ s. At $t = 3$ s, the exoskeleton is commanded to walk at a speed of 0.15 m/s until, at $t = 10$ s, the exoskeleton is commanded to return to a stepping-in-place gait. There is a small steady-state error when forward walking is commanded; this can be attributed to a combination of joint tracking errors from the low-level, proportional-derivative controllers and the compliant (nonrigid) ground being different from the model used for control design. Figure 14 shows the gait-timing variable exhibiting a typical triangle-wave pattern, with leg swapping occurring before $\tau = 1$. It can be seen that, regardless of whether the system was in a periodic gait or transitioning between speeds, τ consistently terminates at approximately 0.9 s. This is due to having trained the system on various transition gaits. The phase portrait in Figure 15 shows the periodic nature of stepping in place, followed by a transient to another periodic condition. The convergence to periodic motion is clear during periods when the speed command is constant. Figure 16 shows stick figures stepping in place, transitioning, and walking forward. An animation of the simulation result can be seen in [67].

Preliminary Robustness Analysis

It is easy to imagine scenarios that could lead to an exoskeleton losing stability and “tripping up,” including unexpected contact with objects in the environment, walking over uneven terrain, external force perturbations being applied on the system, or spasticity (such as involuntary muscle resistance to a patient’s leg motion). In previous work, we evaluated in simulation a PHZD-based controller of the exoskeleton in the face of unexpected slopes and unplanned upper-body motion [53]. Here, we present a preliminary robustness analysis of the machine-learning controller under various external and internal perturbations.

Velocity Perturbations

An analysis in [68] shows that a bipedal robot’s ability to reject velocity perturbations when using HZD-based control strategies correlates with its ability to reject a set of other perturbations, such as variations in terrain height. Based on this observation, it is posited that velocity perturbation rejection provides a reasonable preliminary test of the robustness of the proposed controller framework. In this test, we induce velocity perturbations by applying impulsive external forces of various magnitudes and directions to the exoskeleton

while it is walking. We compare the response of two different closed-loop configurations: one with a controller using the machine learning and another with a fixed, single-periodic gait. The external force is applied at the hip of the exoskeleton during the second step for 0.1 s in either forward or backward directions. When the exoskeleton is commanded to step in place, the results of the Gazebo simulation are shown in Figures 17 and 18. Specifically, using the machine-learning controller, the exoskeleton is able to recover from up to 750 N force in the forward direction and 650 N force in the backward direction. Additionally, when using a controller for a fixed periodic gait, the system lost stability with any forward force larger than 300 N or a backward force larger than 100 N. Figure 17 shows the changes in the forward hip velocity of the exoskeleton for both machine-learning and fixed-gait methods. The supervised machine-learning controller is capable of recovering for relatively large velocity disturbances arising from external forces. Figure 18 shows how the controllers respond to the external disturbances by changing the desired trajectories of the exoskeleton joints. Specifically, the machine-learning controller, when challenged with a large perturbation, extends the swing leg outward by modifying the desired

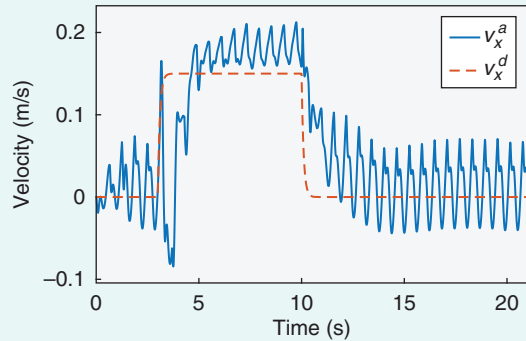


FIGURE 13 The tracking of a desired velocity profile. v_x^a is the actual forward velocity of the pelvis during walking, and v_x^d is the commanded average forward velocity.

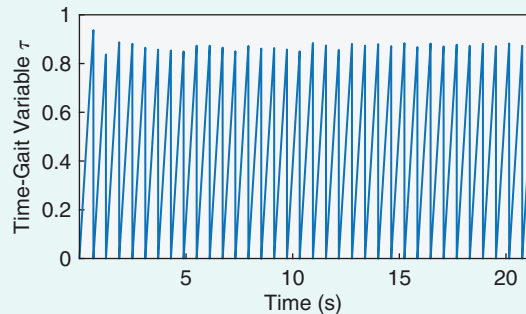


FIGURE 14 The gait-timing variable τ as a function of time, while the exoskeleton follows a varying desired speed.

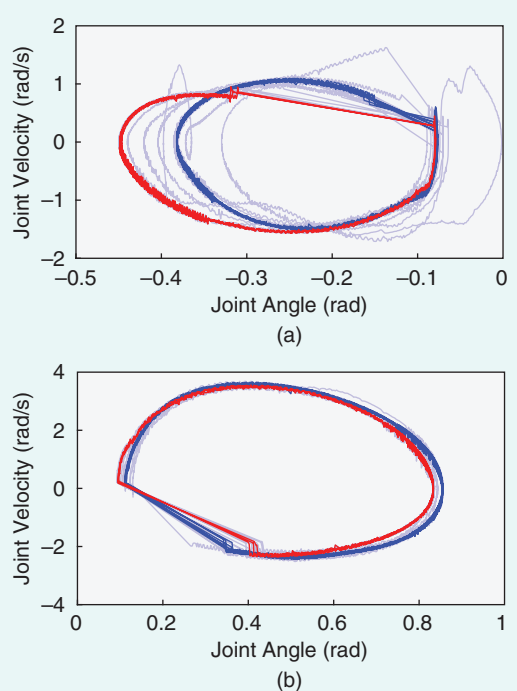


FIGURE 15 The phase portraits of both (a) the swing sagittal hip and (b) the swing knee joints for when the system was tracking a desired velocity profile. Joint angle q versus joint velocity \dot{q} is displayed for the two joints. The solid blue line represents the states in the last quarter of the simulation, while the solid red line represents the part of the simulation in which the exoskeleton reached a steady-state trajectory while walking forward. In both cases, the exoskeleton converged to a periodic cycle.

trajectory of the sagittal swing hip joint. This behavior occurs naturally from training the control surface on optimized walking gaits for various speeds and transitions among them. The fixed-gait controller only uses the large feet of the exoskeleton (regulating the ZMP) to reject the perturbation instead of adjusting the step length. An animation of the velocity perturbation simulations in Gazebo can be seen in [67].

Constant Force Perturbation

While studying velocity perturbation under impulses captures short duration events, such as someone or something bumping into the exoskeleton, it is also interesting to investigate the effects of persistent external forces applied to the system. Figure 19 shows the average speed for when a constant force is applied to the torso 0.5 m above the pelvis under the controller, based on supervised machine learning. The exoskeleton is able to withstand a constant force of ± 75 N for a duration of 10 s. Small drifts in velocity are noticed with the forces applied. The velocities converge to the nominal velocity after the force is removed, with larger forces resulting in a greater loss of stability.

Unplanned forces in the user's legs

A simplified model of spasticity is represented by torques at a user's knee joints. While spasticity occurring simultaneously in both legs was investigated, only spasticity in the right leg is reported here. Both constant and sinusoidal torques are applied, and these are added to the joint-side torque provided by the knee motor and gearing. The mean absolute error (MAE) in joint tracking is computed for the right knee. It is observed that the MAE increases only slightly, as shown in Table 4. Additionally, no differences in the gaits are visually observed.

PRELIMINARY EXPERIMENTAL RESULTS USING PARTIAL HYBRID ZERO DYNAMICS

Experimental implementation of the biped-inspired control laws has begun, with very promising results, as alluded to in the opening paragraph of this article. Because the PHZD control laws have been extensively evaluated on several bipedal robot platforms, they have been employed in the initial testing. The results described below were first reported in [54], where a video of patients using the exoskeleton can be found.

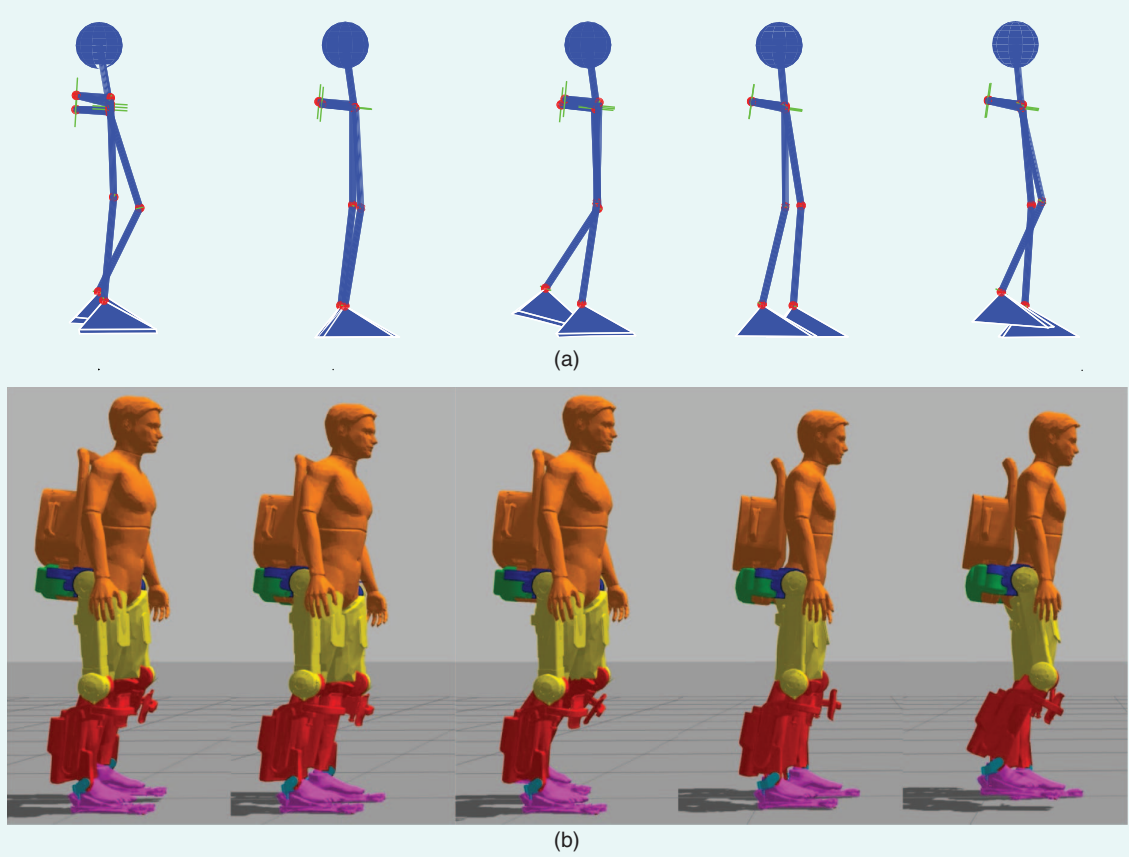


FIGURE 16 The outtakes from animations of the exoskeleton tracking a desired velocity profile. (a) Stick figures are added for clarity with the same motion as the images in (b) from the Gazebo simulation. The first two images show the step-in-place gait. The third image shows how the system looks like when it is starting to transition. The last two show the exoskeleton walking forward in a periodic gait.

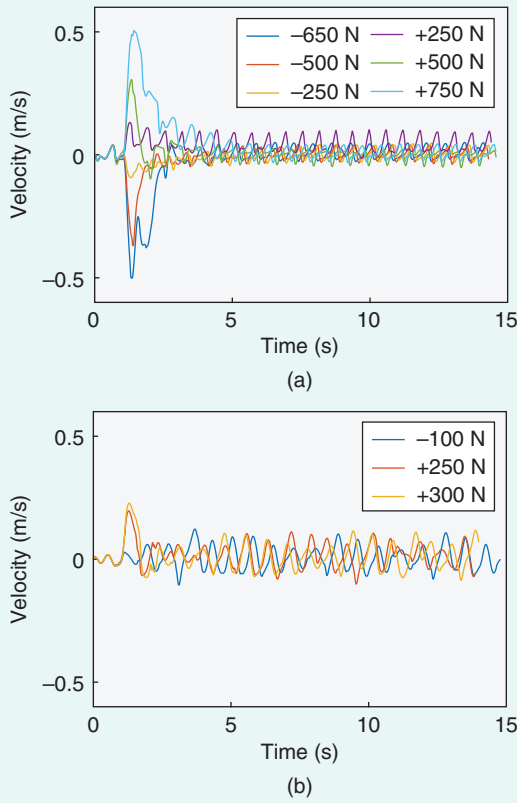


FIGURE 17 The change in hip velocity due to a perturbation. Part (a) shows that the control algorithm based on supervised machine learning is able to recover from larger perturbations. Part (b) shows the fixed gait. Both controllers failed under perturbations larger than those shown.

In the first evaluation of the controllers, a mannequin or dummy was placed in the exoskeleton (see Figure 20). As shown in Figure 21, the nominal and target trajectories (in red and blue, respectively) are marginally different after the tuning and high-level filtering of the nominal trajectories. The target gait is followed with relatively good accuracy, resulting in stable dynamic walking of the hardware.

Experimental Results with Human Subjects

Due to the successful results obtained with the mannequin, experiments are conducted with paraplegic patients. All patients are complete paraplegics, unable to stand by themselves or walk, with lesions ranging from T12 to T6. Some characteristics of these patients are summarized in Table 5.

Experiments were conducted in a certified medical center and approved by the ANSM (the French regulatory administration for health products). To prevent injury from a fall, one person is placed on each side of a patient. In case of a loss of balance, the two assistants catch the exoskeleton using the handles on its sides. A safety cable is attached to the exoskeleton and an overhead rail (or gantry). This is a

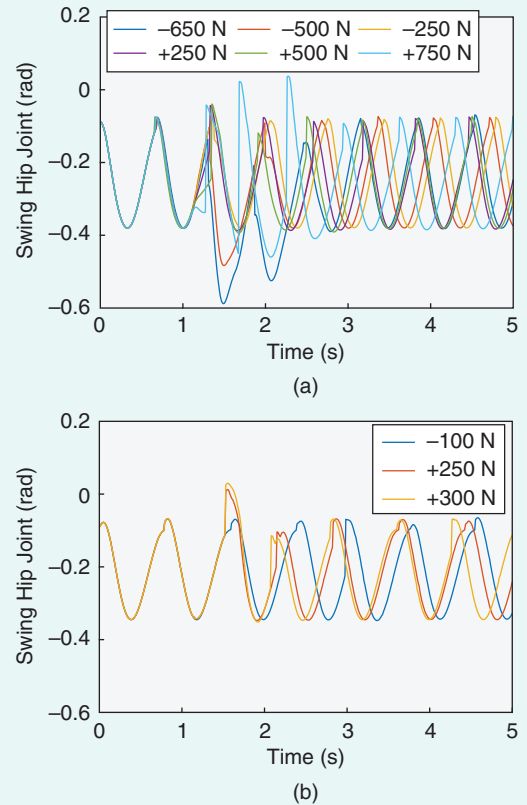


FIGURE 18 The swing hip joint angle as a function of time while responding to a perturbation. (a) Supervised machine learning and (b) fixed gait. (a) When experiencing large perturbations, the controller based on supervised machine learning makes more use of its swing foot to return to a stepping-in-place gait.

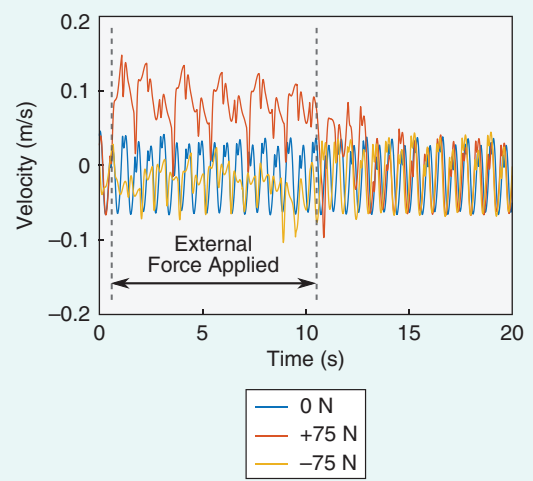


FIGURE 19 The instantaneous velocity of the hip when the system is perturbed for a duration of 10 s. The forward push causes the system to drift slightly more while the force is being applied. When the force is removed, the velocity converges back to the nominal velocity.

secondary means to secure a patient and prevent a fall. Assistance is provided only in case of loss of balance; during walking, the exoskeleton and its user are self-stabilized, and no outside assistance was given.

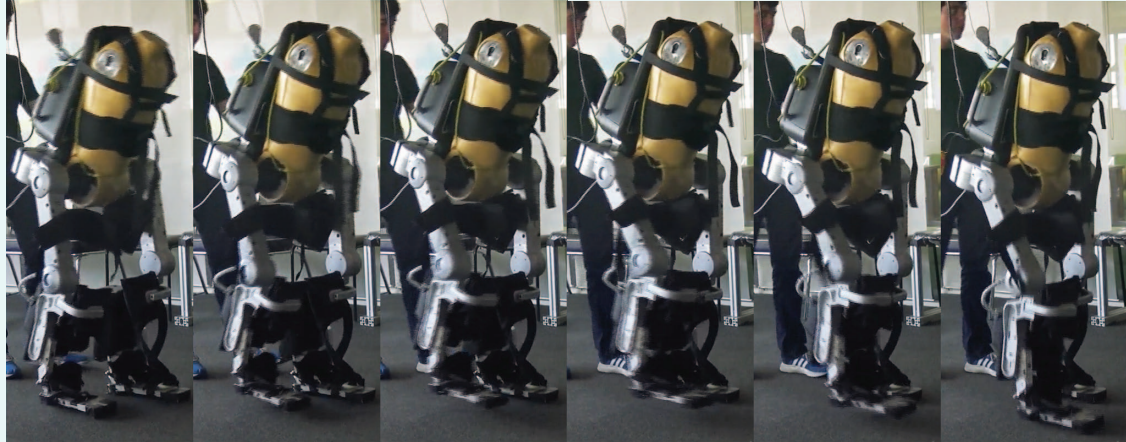
As can be seen in Figure 22, which shows tiles from the video in [54], crutchless, dynamically stable exoskeleton walking of paraplegic patients is achieved as a result of the methodology developed for bipedal robots. All patients managed to walk unassisted for the entire length of the room after a few trials, during which a best gait was chosen and then tuned. Table 5 includes the speed of walking and the distance traveled.

The ability to successfully transfer the formal gaits generated to hardware is illustrated in Figure 23 for patient A, wherein the nominal (blue) and measured (shaded) trajectories are consistent throughout the experiment. The tracking error at the joint level for patient A can be seen in Figure 24. The motor torques resulting from tracking the nominal trajectories (Figure 25) are also consistent with simulation. Note that motor-torque saturations are relatively uncommon since the gaits are designed to

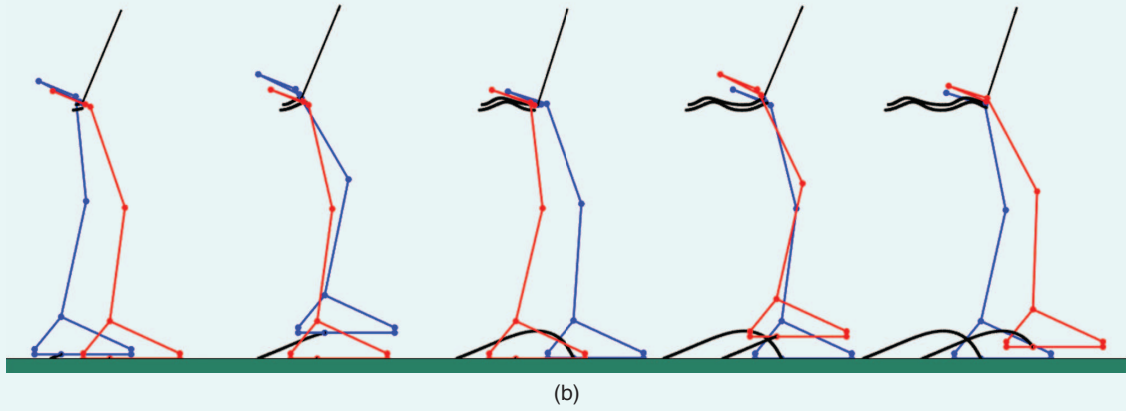
TABLE 4 The mean absolute error (MAE) for joint angle tracking when applying external torques on the right knee joint, which represents a simplified model of spasticity.

Test	MAE (rad) at Steady State
No perturbations	0.013
A constant +100-Nm torque	0.0166
A constant -100-Nm torque	0.018
A sinusoidal 100-Nm torque at a 1-Hz frequency	0.0147
A sinusoidal 100-Nm torque at a 10-Hz frequency	0.0154

account for all of the hardware limits. To compare the walking gaits among patients, a representative selection of phase portraits for each patient is presented in Figure 26. Even though the gaits are not the same (as they have been generated to best suit each patient), they all display a common fundamental structure. This is further illustrated



(a)



(b)

FIGURE 20 The tiled snapshot images of the nominal gait from the optimization of the exoskeleton with a mannequin inside, (a) in experiment and (b) in simulation. The black lines in the simulation images show the evolution of the pelvis and swing sole positions.

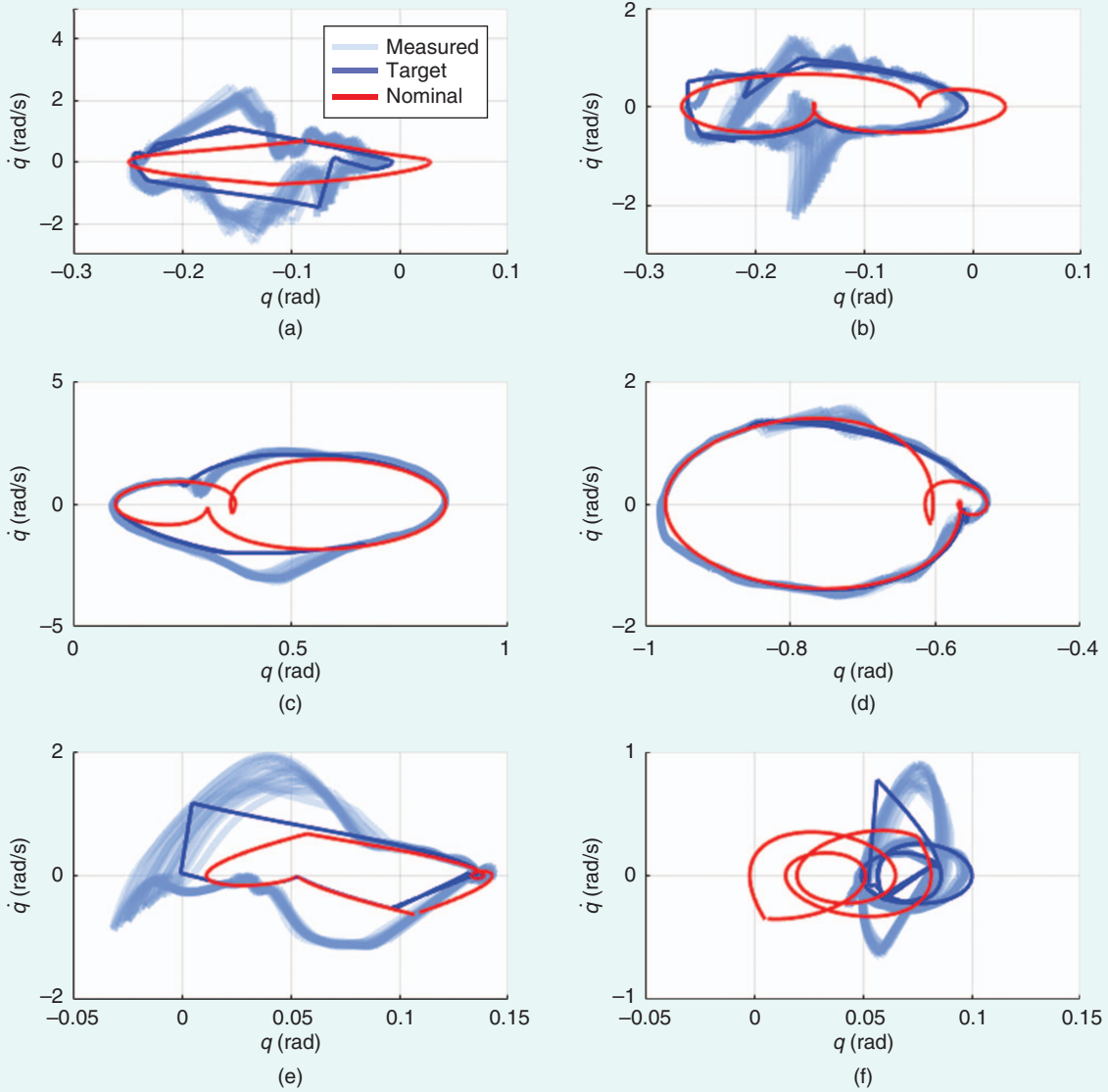


FIGURE 21 The phase portraits for the dummy during 20 s of unassisted walking [54]: (a) left Henke ankle, (b) left sagittal ankle, (c) left sagittal knee, (d) left sagittal hip, (e) left transverse hip, and (f) left frontal hip. Red is the nominal orbit from optimization, while blue is the “tuned” orbit to account for the mechanical imperfections and compliances of the robot.

TABLE 5 The patient data. The selection criteria included being unable to stand by oneself, being able to remain seated on a chair without further assistance, having no ambulatory ability before using the exoskeleton, and low-to-moderate spasticity allowed.

Patient	Height (m)	Weight (kg)	Distance	
			Traveled (m)	Speed (m/s)
A	1.8	68	8.9	0.11
B	1.69	80	10.56	0.15
C	1.8	75	9.5	0.13

in gait tiles of the patients walking in the exoskeleton (Figure 22).

Next Steps

While the dynamic walking gaits obtained are preliminary and in no way constitute any kind of clinical evaluation, the ability to consistently realize them on patients points toward the validity of the framework being pursued. During the preliminary testing, the few tests that failed to completely traverse the lab were caused by foot scuffing or loss of lateral balance. In the next phase of testing, we will evaluate the G-HZD controllers discussed in the previous two sections.

FUTURE WORK

While this article presents an important accomplishment, much remains to be done in the field of actively controlled exoskeletons. Future research directions involve developing control algorithms that 1) directly address model uncertainty; 2) support a rich set of behaviors, such as standing and sitting and dynamic transitions between these; 3) enable push recovery and robustness to significantly force disturbances that could arise due to contact with the environment

or other humans; 4) use models of human comfort to balance between comfort and robustness of a gait of the exoskeleton; 5) capture human intent to enable human-driven autonomous exoskeleton control; 6) adapt to and provide user customized behaviors; and 7) improve the energy efficiency of assisted walking. Regarding model uncertainty, it is hoped that methods developed in [68] can be incorporated into the optimization and machine-learning methods to provide robust nominal orbits.



(a)



(b)



(c)

FIGURE 22 The walking tiles of (a) patient A, (b) patient B, and (c) patient C.

We believe methods presented in this article can be extended to tackle many of these tasks. For example, Figure 27 shows preliminary results for a transition from sitting to standing obtained via optimization. In the model, it was assumed that users can use their arms to assist liftoff by applying an external force on the chair up to half of their body weight. It can be seen from Figure 28 that most of the force is used to push the user horizontally off the chair.

SUMMARY REMARKS

The ATALANTE exoskeleton studied in this article is the first to allow dynamic hands-free walking for paraplegics. Where other devices require crutches for lateral stabilization, the embedded control algorithms on the studied exoskeleton regulate leg motion to sustain a locally exponen-

tially stable walking gait. The keys to realizing crutchless dynamic walking were novel hardware (stiff enough to physically support a subject and powerful enough to move the device's legs quickly) and novel control mathematics developed over the past 15 years to allow bipedal robots to walk stably in uncertain environments and with imprecise dynamic models.

The preliminary experimental results have demonstrated very slow walking on the order of 0.1 m/s. Stable gaits at 0.4 m/s have been achieved in simulation, and such speeds can be expected to be reached on the current hardware and with patients. New tools are becoming available for the rapid computation of trajectories for high-DOF mechanical systems as well as new control methods that are providing ways to mitigate the curse of dimensionality. A path forward to restoring locomotion for paraplegics is becoming clearer.

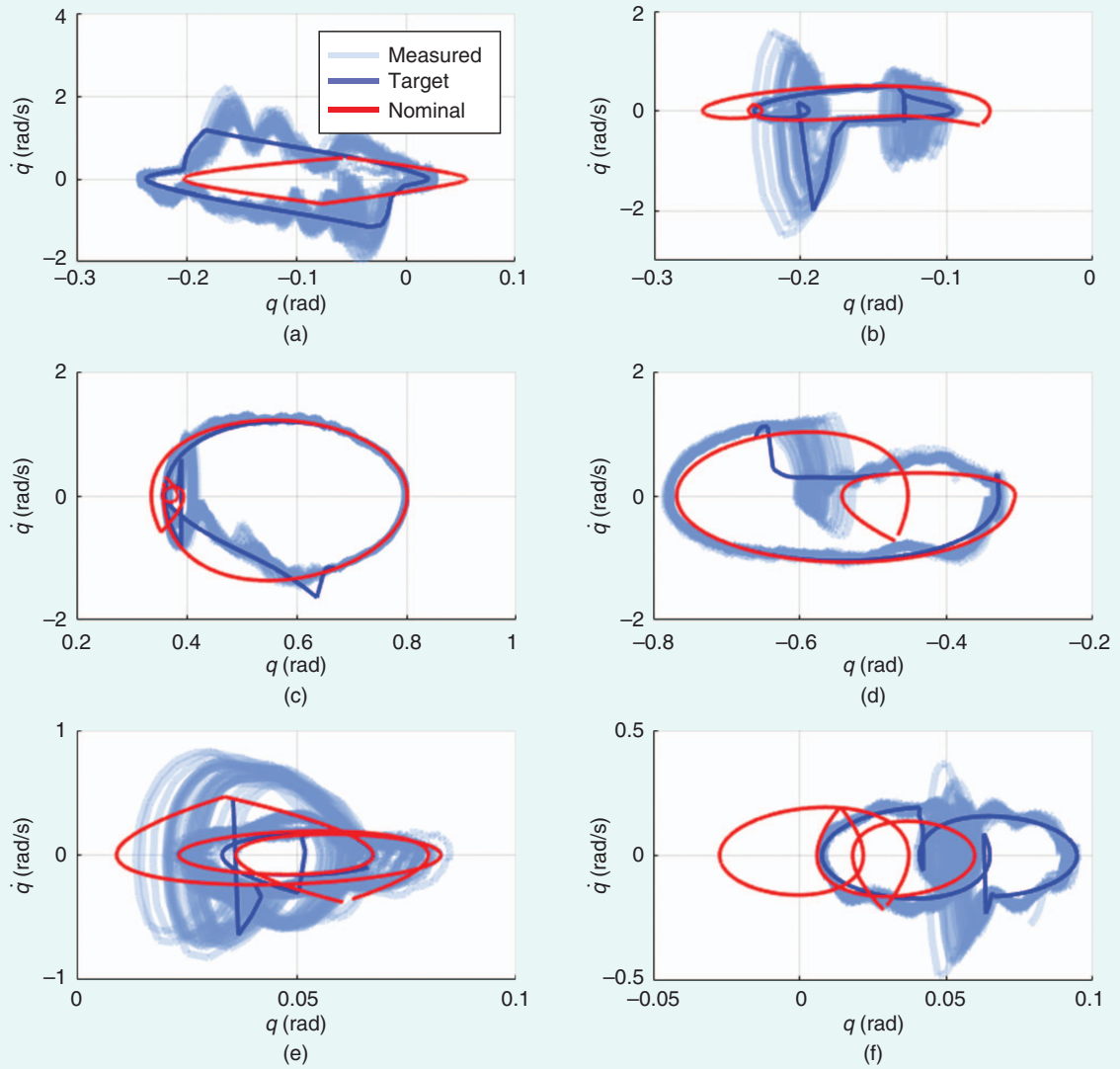


FIGURE 23 The phase portraits for patient A during 60 s of unassisted walking: (a) left Henke ankle, (b) left sagittal ankle, (c) left sagittal knee, (d) left sagittal hip, (e) left transverse hip, and (f) left frontal hip.

ACKNOWLEDGMENTS

The U.S. investigators are covered under IRB Protocol Number 16-0693. The French investigators are covered under CPP Ile de France XI, Number 16041. The authors thank the entire Wandercraft team who designed ATALANTE and implemented and tested the control algorithms used in the experiments. Additionally, the authors are grateful to Laurent Praly and Nicolas Petit, researchers at CAS (Mines ParisTech, PSL Research University) for their scientific support since the founding of Wandercraft. The

authors thank Xingye (Dennis) Da for his consultation on G-HZD. The work of A. Hereid was supported by the National Science Foundation (NSF) under Grant CPS-1239037. The work of O. Harib and J.W. Grizzle was supported in part by NSF Grant NRI-1525006 and in part by a gift from Ford Motor Company. M.E. Mungai is supported by a University of Michigan, Ann Arbor, fellowship. The work of A. Agrawal and K. Sreenath is supported by NSF Grant IIS-1526515. The work of T. Gurriet and A.D. Ames was supported by NSF NRI Award 1526519.

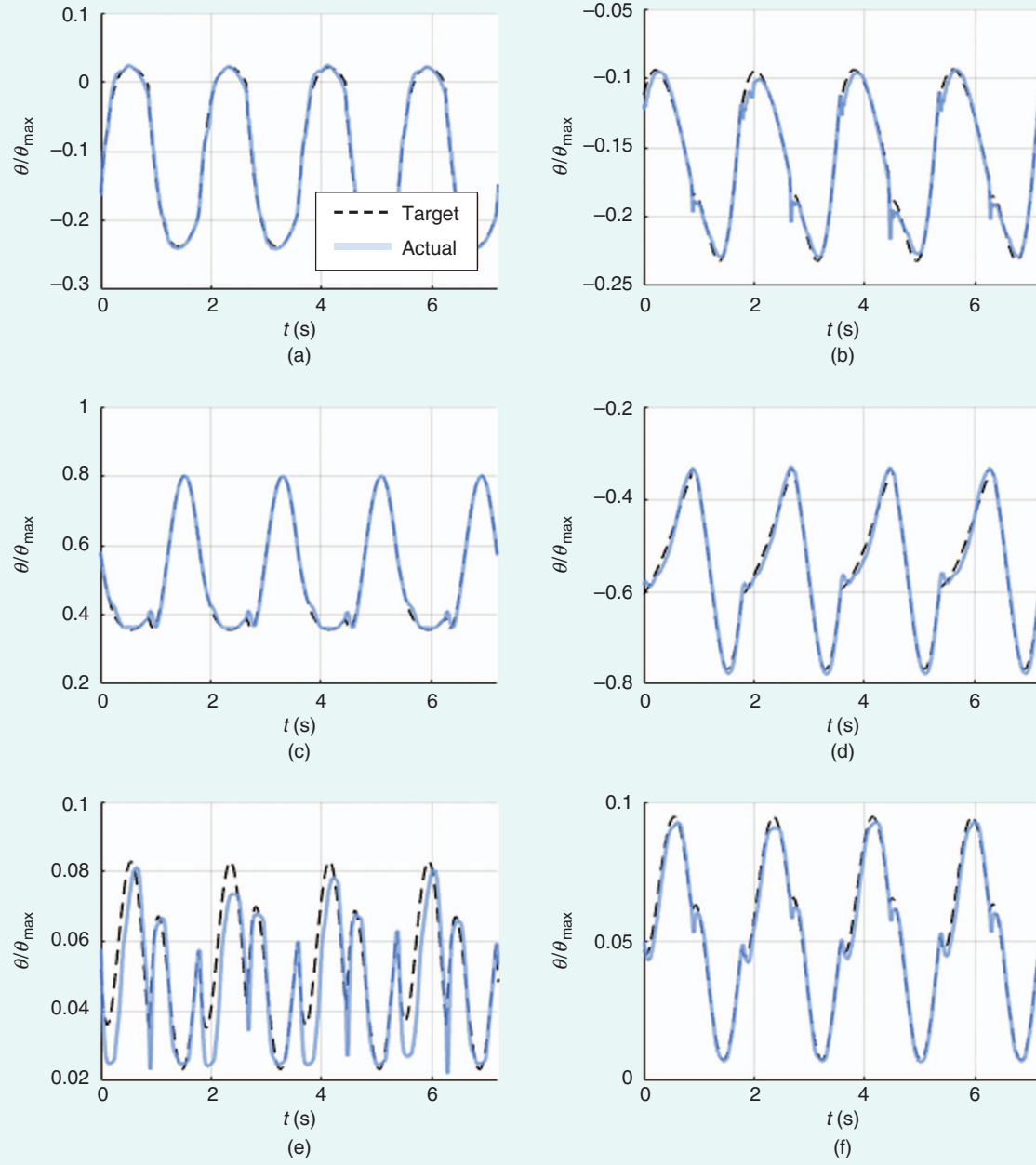


FIGURE 24 A selection of normalized tracking performances of the local controllers at the joint for patient A: (a) left Henke ankle, left sagittal ankle, (c) left sagittal knee, (d) left sagittal hip, (e) left transverse hip, and (f) left frontal hip.

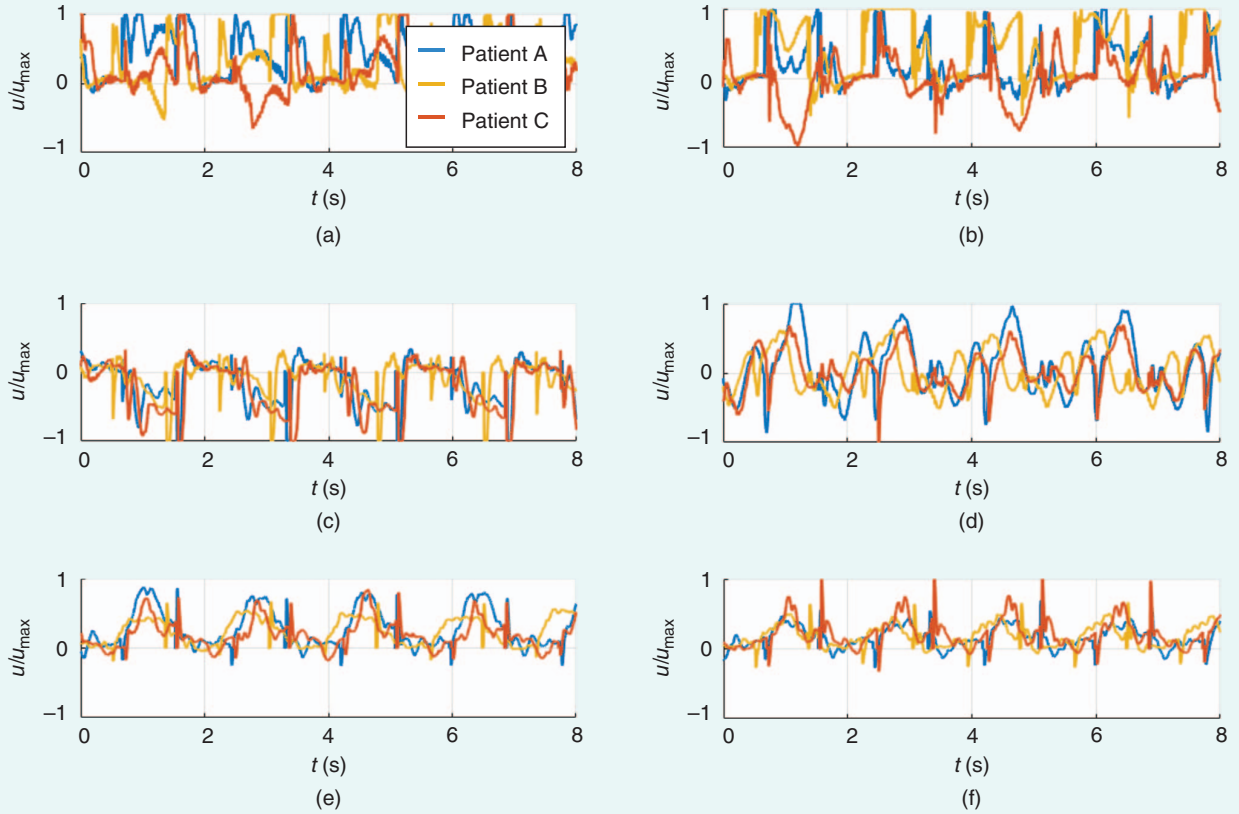


FIGURE 25 The normalized experimental motor torques for three different patients [54]. Other than for patient B, the motor torques rarely saturate; the result is reserve torque for responding to disturbances. (a) Left Henke ankle, (b) left sagittal ankle, (c) left sagittal knee, (d) left sagittal hip, (e) left transverse hip, and (f) left frontal hip.

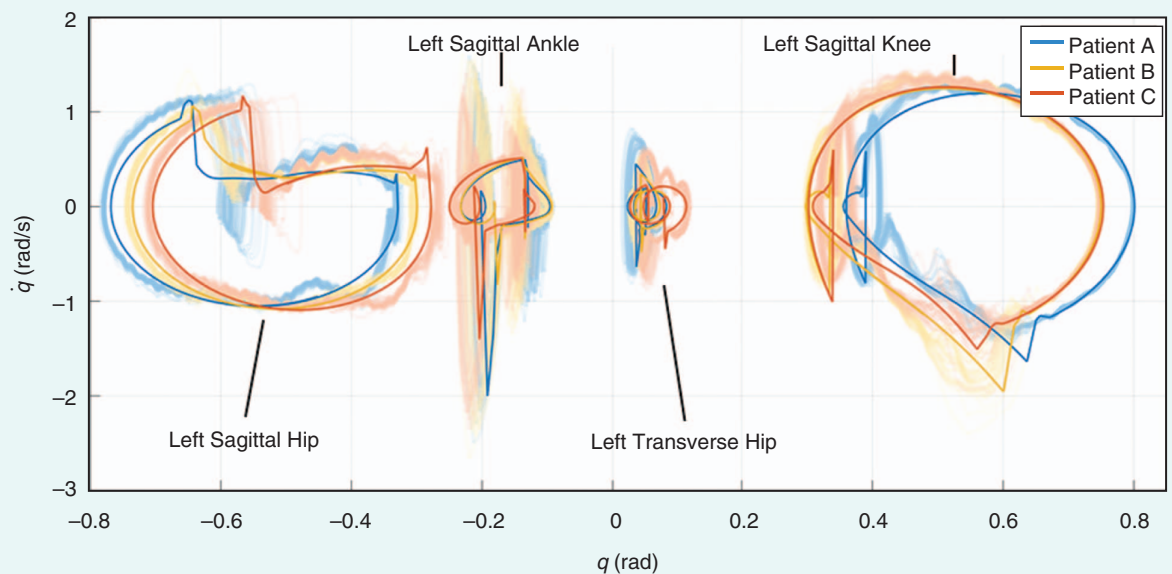


FIGURE 26 A selection of phase portraits. The solid lines are the target trajectories, and the shaded regions are the measured joint positions.

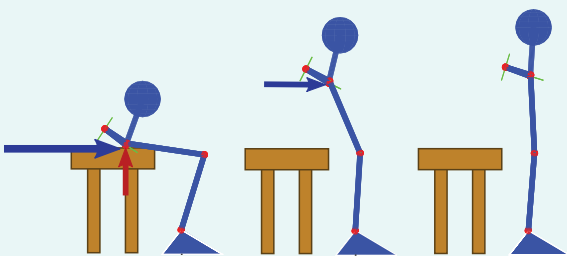


FIGURE 27 The stick figure animation of an exoskeleton user transitioning from sitting to standing. The first image is at $t = 0\text{ s}$, the second image is at $t = 0.6\text{ s}$, and the third image is at $t = 1.8\text{ s}$. The blue and red arrows show external forces applied to the system through the user's arms. In the optimization, it is assumed that users can exert up to half of their body weight as an external force.

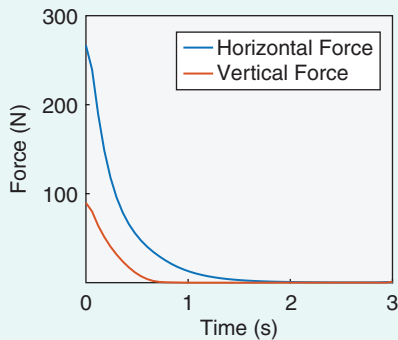


FIGURE 28 The force exerted by the user to assist in standing up. The exoskeleton is upright after 1.8 s.

AUTHOR INFORMATION

Omar Harib (oharib@umich.edu) is a Ph.D. candidate in electrical and computer engineering at the University of Michigan, Ann Arbor. He received B.S. degrees in mechanical engineering and computer engineering at the American University of Sharjah, United Arab Emirates. His current research interests are in control theory and experimentation focusing on bipedal robot locomotion. He can be contacted at 1301 Beal Avenue, Ann Arbor, Michigan 48109-2122.

Ayonga Hereid received the Ph.D. degree in mechanical engineering from the Georgia Institute of Technology, Atlanta, in 2016. He is currently a postdoctoral research fellow in the Department of Electrical Engineering and Computer Science at the University of Michigan, Ann Arbor. He received the DENSO Best Student Paper Award of the 17th International Conference on Hybrid Systems: Computation and Control in 2014. His current research interests include developing advanced nonlinear optimization and control algorithms to realize dynamic and natural locomotion on bipedal robots.

Ayush Agrawal received the M.S. degree in mechanical engineering from Carnegie Mellon University, Pittsburgh,

Pennsylvania, in 2017 and a B.Tech. degree in mechanical engineering from the National Institute of Technology, Karnataka, India, in 2015. He is currently a Ph.D. student in the Department of Mechanical Engineering at the University of California, Berkeley, and is part of the Hybrid Robotics Laboratory. His research interests include the areas of nonlinear control and bipedal locomotion.

Thomas Gurriet earned a degree from Arts et Métiers ParisTech, France, and the M.S. degree in mechanical engineering from the Georgia Institute of Technology, Atlanta, in 2015. He is currently pursuing a Ph.D. degree in the Department of Mechanical and Civil Engineering at the California Institute of Technology, Pasadena. His current research interests are in safety critical control.

Sylvain Finet earned a degree from ENSTA ParisTech, France, in 2013 and the Ph.D. degree in bipedal robotics at Mines ParisTech, France, in 2017. He currently works as a control engineer at Wandercraft. He joined Wandercraft at its inception and is currently a control engineer there. His current research interests include theoretical and experimental aspects of nonlinear control and bipedal robotics.

Guilhem Boéris earned a degree from Ecole Polytechnique, Palaiseau, Paris, in 2011 and the M.S. degree in theoretical physics at Ecole Normale Supérieure de Paris, in 2012. As a Ph.D. student, he worked on quantum Monte Carlo methods to study superfluid phase transitions in disordered Bose gases. He currently works as a control engineer at Wandercraft, where his research interests include theoretical and experimental aspects of nonlinear control and bipedal locomotion.

Alexis Duburcq received the M.S. degree in microengineering from Ecole Polytechnique Fédérale de Lausanne, France, in 2017 and a degree from Ecole Centrale, Paris, in 2017. He is currently a Ph.D. student in robotics and computer engineering at the University of Dauphine, Paris, France. In 2017, he joined Wandercraft, where he is working on hybrid zero dynamics gait optimization. His current research interests include machine learning applied to locomotion for exoskeletons.

M. Eva Mungai received the B.S. degree in mechanical engineering at Rensselaer Polytechnic Institute, Troy, New York, in 2017. She is currently pursuing the M.S. and Ph.D. degrees in mechanical engineering at the University of Michigan, Ann Arbor. Her research interests include control theory and experiments for bipedal locomotion and standing and sitting for bipedal robots.

Matthieu Masselin received a degree from the Ecole Polytechnique, Fédérale de Lausanne, France, and an M.S. degree in electrophysics from Kungliga Tekniska Högskolan Royal Institute of Technology, Stockholm, Sweden, in 2013. He is currently with Wandercraft, where he has been developing the control team. He has led an effort to implement dynamic walking on the Wandercraft exoskeleton, building on knowledge developed for biped robots.

Aaron D. Ames earned the B.S. and B.A. degrees in mechanical engineering and mathematics, respectively, from the University of St. Thomas, St. Paul, Minnesota, in 2001 and the M.A. and Ph.D. degrees in mathematics and electrical engineering and computer sciences, respectively, from the University California (UC), Berkeley, in 2006. He is currently the Bren Professor of Mechanical and Civil Engineering and Control and Dynamical Systems at the California Institute of Technology (Caltech), Pasadena. Prior to joining Caltech in 2017, he was an associate professor at the Georgia Institute of Technology, Atlanta, in the Woodruff School of Mechanical Engineering and the School of Electrical and Computer Engineering. He served as a postdoctoral scholar in Control and Dynamical Systems at Caltech from 2006 to 2008 and began his faculty career at Texas A&M University, College Station, in 2008. At UC Berkeley, he was the recipient of the 2005 Leon O. Chua Award for achievement in nonlinear science, the 2006 Bernard Friedman Memorial Prize in Applied Mathematics, the National Science Foundation CAREER Award in 2010, and the 2015 Donald P. Eckman Award. His research interests span the areas of robotics, nonlinear control, and hybrid systems, with a special focus on applications to bipedal robotic walking, both formally and through experimental validation. His lab designs, builds, and tests novel bipedal robots, humanoids, and prostheses with the goal of achieving human-like bipedal robotic locomotion and translating these capabilities to robotic-assistive devices.

Koushil Sreenath received the M.S. degree in applied mathematics and a Ph.D. degree in electrical engineering and computer science from the University of Michigan, Ann Arbor, in 2011. He is currently an assistant professor of mechanical engineering at the University California (UC), Berkeley. Prior to joining UC Berkeley, he was a postdoctoral scholar at the GRASP Laboratory at the University of Pennsylvania, Philadelphia, from 2011 to 2013 and an assistant professor at Carnegie Mellon University, Pittsburgh, Pennsylvania, from 2013 to 2017. He received the Best Paper Award at the Robotics: Science and Systems Conference in 2013 and the Google Faculty Research Award in Robotics in 2015. His research interests lie at the intersection of highly dynamic robotics and applied nonlinear control.

Jessy W. Grizzle received the Ph.D. degree in electrical engineering from The University of Texas at Austin in 1983. He is currently a professor of electrical engineering and computer science at the University of Michigan, Ann Arbor, where he holds the titles of the Elmer Gilbert Distinguished University Professor and the Jerry W. and Carol L. Levin Professor of Engineering. He is also the director of Michigan Robotics. He is a co-inventor on 16 patents dealing with emissions reduction in passenger vehicles through improved control system design. He received the Paper of the Year Award from the IEEE Vehicular Technology Society in 1993, the George S. Axelby Award in 2002, the Control Systems Technology Award in 2003, the Bode Prize in 2012, and the IEEE Transactions on Control Systems Tech-

nology Outstanding Paper Award in 2014. His work on bipedal locomotion has been the subject of numerous plenary lectures and has been featured on CNN, ESPN, and the Discovery Channel and in *The Economist*, *Wired Magazine*, *Discover Magazine*, *Scientific American*, and *Popular Mechanics*. He is a Fellow of the IEEE and the International Federation of Automatic Control.

REFERENCES

- [1] Wandercraft. Accessed on: Nov. 7, 2017. [Online]. Available: <http://www.wandercraft.eu/en/>
- [2] A. M. Dollar and H. Herr, "Lower extremity exoskeletons and active orthoses: Challenges and state of the art," *IEEE Trans. Robot.*, vol. 24, no. 1, pp. 144–158, 2008.
- [3] K. Ziegler-Graham, E. J. MacKenzie, P. L. Ephraim, T. G. Travison, and R. Brookmeyer, "Estimating the prevalence of limb loss in the United States: 2005 to 2050," *Arch. Phys. Med. Rehabil.*, vol. 89, no. 3, pp. 422–429, 2008. doi:10.1016/j.apmr.2007.11.005.18295618.
- [4] R. L. Waters, J. Perry, D. Antonelli, and H. Hislop, "Energy cost of walking of amputees: The influence of level of amputation," *J. Bone Joint Surg. Amer.*, vol. 58, no. 1, pp. 42–46, 1976.
- [5] J. P. Pell, P. T. Donnan, F. G. Fowkes, and C. V. Ruckley, "Quality of life following lower limb amputation for peripheral arterial disease," *Eur. J. Vasc. Surg.*, vol. 7, no. 4, pp. 448–451, 1993.
- [6] W. Miller, A. Deathe, M. Speechley, and J. Koval, "The influence of falling, fear of falling, and balance confidence on prosthetic mobility and social activity among individuals with a lower extremity amputation," *Arch. Phys. Med. Rehabil.*, vol. 82, no. 9, pp. 1238–1244, 2001. doi: 10.1053/apmr.2001.25079.
- [7] H. I. Krebs, N. Hogan, M. L. Aisen, and B. T. Volpe, "Robot-aided neurorehabilitation," *IEEE Trans. Rehabil. Eng.*, vol. 6, no. 1, pp. 75–87, 1998.
- [8] P. R. Geigle and M. Kallins, "Exoskeleton-assisted walking for people with spinal cord injury," *Arch. Phys. Med. Rehabil.*, vol. 98, no. 7, pp. 1493–1495, 2017. doi:10.1016/j.apmr.2016.12.002.18185638.
- [9] A. M. Dollar and H. Herr, "Lower extremity exoskeletons and active orthoses: Challenges and state of the art," *IEEE Trans. Robot.*, vol. 24, no. 1, pp. 144–158, 2008.
- [10] A. J. Young and D. P. Ferris, "State of the art and future directions for lower limb robotic exoskeletons," *IEEE Trans. Neural Syst. Rehabil. Eng.*, vol. 25, no. 2, pp. 171–182, 2017.
- [11] W. Huo, S. Mohammed, J. C. Moreno, and Y. Amirat, "Lower limb wearable robots for assistance and rehabilitation: A state of the art," *IEEE Syst. J.*, vol. 10, no. 3, pp. 1068–1081, 2016.
- [12] R. S. Mosher, "Handyman to hardiman," SAE, Warrendale, PA, Tech. Rep. 670088, 1967.
- [13] J. Grundmann and A. Seireg, "Computer control of multi-task exoskeleton for paraplegics," in *Proc. 2nd CISM/IFTOMM Int. Symp. Theory and Practice of Robots and Manipulators*, 1977, pp. 233–240.
- [14] M. Vukobratovic, D. Hristic, and Z. Stojiljkovic, "Development of active anthropomorphic exoskeletons," *Med. Biol. Eng.*, vol. 12, no. 1, pp. 66–80, 1974.
- [15] D. Hristic, M. Vukobratovic, and M. Timotijevic, "New model of autonomous' active suit for dystrophic patients," in *Proc. Int. Symp. External Control of Human Extremities*, 1981, pp. 33–42.
- [16] Ekso Bionics. Accessed on: Nov. 4, 2017. [Online]. Available: <http://eksobionics.com/>
- [17] ReWalk 6.0—Home. Accessed on: Nov. 4, 2017. [Online]. Available: <http://rewalk.com/>
- [18] G. Zeilig, H. Weingarden, M. Zwecker, I. Dudkiewicz, A. Bloch, and A. Esquenazi, "Safety and tolerance of the ReWalk exoskeleton suit for ambulation by people with complete spinal cord injury: A pilot study," *J. Spinal Cord Med.*, vol. 35, no. 2, pp. 96–101, 2012. doi:10.1179/2045772312Y.0000000003.
- [19] K. Suzuki, G. Mito, H. Kawamoto, Y. Hasegawa, and Y. Sankai, "Intention-based walking support for paraplegia patients with robot suit HAL," *Adv. Robot.*, vol. 21, no. 12, pp. 1441–1469, 2007.
- [20] Cyberdyne. Accessed on: Nov. 6, 2017. [Online]. Available: https://www.cyberdyne.jp/english/products/LowerLimb_medical.html
- [21] R. Jimenez-Fabian and O. Verlinden, "Review of control algorithms for robotic ankle systems in lower-limb orthoses, prostheses, and exoskeletons," *Med. Eng. Phys.*, vol. 34, no. 4, pp. 397–408, 2012.
- [22] F. Sup, A. Bohara, and M. Goldfarb, "Design and control of a powered trans-femoral prosthesis," *Int. J. Robot. Res.*, vol. 27, no. 2, pp. 263–273, 2008.
- [23] A. Simon, N. Fey, S. Finucane, R. Lipschutz, and L. Hargrove, "Strategies to reduce the configuration time for a powered knee and ankle prosthesis across

- multiple ambulation modes," in *Proc. IEEE Int. Conf. Rehabilitation Robotics*, 2013, pp. 1–6.
- [24] A. M. Simon, K. A. Ingraham, N. P. Fey, S. B. Finucane, R. D. Lipschutz, A. J. Young, and L. J. Hargrove, "Configuring a powered knee and ankle prosthesis for transfemoral amputees within five specific ambulation modes," *PLoS One*, vol. 9, no. 6, pp. e99387, 2014. doi: 10.1371/journal.pone.0099387.
- [25] R. D. Gregg, T. Lenzi, L. J. Hargrove, and J. W. Sensinger, "Virtual constraint control of a powered prosthetic leg: From simulation to experiments with transfemoral amputees," *IEEE Trans. Robot.*, vol. 30, no. 6, pp. 1455–1471, 2014.
- [26] E. Stickland, "Good-bye, wheelchair," *IEEE Spectr.*, vol. 49, no. 1, pp. 30–32, 2012.
- [27] R. Angold, N. Harding, and H. Kazerooni, "Semi-powered lower extremity exoskeleton," U.S. Patent 8057410, Nov. 2011.
- [28] K. Anam and A. A. Al-Jumaily, "Active exoskeleton control systems: State of the art," in *Proc. Int. Symp. Robotics and Intelligent Sensors (IRIS)*, pp. 988–994, 2012.
- [29] M. R. Tucker, J. Olivier, A. Pagel, H. Bleuler, M. Bouri, O. Lamberty, J. del R. Millán, R. Riener, H. Vallery, and R. Gassert, "Control strategies for active lower extremity prosthetics and orthotics: A review," *J. NeuroEng. Rehabil.*, vol. 12, no. 1, pp. 1, 2015. doi: 10.1186/1743-0003-12-1.
- [30] K. Suzuki, G. Mito, H. Kawamoto, Y. Hasegawa, and Y. Sankai, "Intention-based walking support for paraplegia patients with robot suit HAL," *Adv. Robot.*, vol. 21, no. 12, pp. 1441–1469, 2007.
- [31] G. Aguirre-Ollinger, J. Colgate, M. Peshkin, and A. Goswami, "Active-impedance control of a lower-limb assistive exoskeleton," in *Proc. IEEE Int. Conf. Rehabilitation Robotics*, 2007, pp. 188–195.
- [32] M. Gomes, G. Silveira, and A. Siqueira, "Gait pattern adaptation for an active lower-limb orthosis based on neural networks," *Adv. Robot.*, vol. 25, no. 15, pp. 1903–1925, 2011.
- [33] T. Nef, M. Guidali, and R. Riener, "ARMin III-arm therapy exoskeleton with an ergonomic shoulder actuation," *Appl. Bionics Biomechanics*, vol. 6, no. 2, pp. 127–142, 2009.
- [34] A. Frisoli, E. Sotgiu, C. Procopio, M. Bergamasco, B. Rossi, and C. Chisari, "Design and implementation of a training strategy in chronic stroke with an arm robotic exoskeleton," in *Proc. IEEE Int. Conf. Rehabilitation Robotics*, 2011, pp. 1–8.
- [35] S. Jezernik, G. Colombo, T. Keller, H. Frueh, and M. Morari, "Robotic orthosis Lokomat: A rehabilitation and research tool," *Neuromodulation: Technol. Neural Interface*, vol. 6, no. 2, pp. 108–115, 2003. doi: 10.1046/j.1525-1403.2003.0017.x.
- [36] A. Tsukahara, Y. Hasegawa, and Y. Sankai, "Gait support for complete spinal cord injury patient by synchronized leg-swing with HAL," in *Proc. IEEE/RSJ Int. Conf. Intelligent Robots and Systems*, 2011, pp. 1737–1742.
- [37] O. Unluhisarcikli, M. Pietrusinski, B. Weinberg, P. Bonato, and C. Mavroidis, "Design and control of a robotic lower extremity exoskeleton for gait rehabilitation," in *Proc. IEEE/RSJ Int. Conf. Intelligent Robots and Systems*, 2011, pp. 4893–4898.
- [38] E. Wolbrecht, D. Reinkensmeyer, and J. Bobrow, "Pneumatic control of robots for rehabilitation," *Int. J. Robot. Res.*, vol. 29, no. 1, pp. 23–38, 2010.
- [39] E. Rocon, J. Belda-Lois, A. Ruiz, M. Manto, J. Moreno, and J. Pons, "Design and validation of a rehabilitation robotic exoskeleton for tremor assessment and suppression," *IEEE Trans. Neural Syst. Rehabil. Eng.*, vol. 15, no. 3, pp. 367–378, 2007.
- [40] K. Sreenath, H. Park, I. Poulakakis, and J. W. Grizzle, "Embedding active force control within the compliant hybrid zero dynamics to achieve stable, fast running on MABEL," *Int. J. Robot. Res.*, vol. 32, no. 3, pp. 324–345, 2013. doi: 10.1177/0278364912473344.
- [41] S. Feng, E. Whitman, X. Xinjilefu, and C. G. Atkeson, "Optimization-based full body control for the DARPA Robotics Challenge," *J. Field Robot.*, vol. 32, no. 2, pp. 293–312, 2015.
- [42] S. Kuindersma, F. Permenter, and R. Tedrake, "An efficiently solvable quadratic program for stabilizing dynamic locomotion," in *Proc. IEEE Int. Conf. Robotics and Automation (ICRA)*, 2014, pp. 2589–2594.
- [43] H. Dai, A. Valenzuela, and R. Tedrake, "Whole-body motion planning with centroidal dynamics and full kinematics," in *Proc. 14th IEEE-RAS Int. Conf. Humanoid Robots*, 2014, pp. 295–302.
- [44] T. Koolen, J. Smith, G. Thomas, S. Bertrand, J. Carff, N. Mertins, D. Stephen, P. Abeles, J. Englsberger, S. McCrary, J. van Egmond, M. Griffioen, M. Floyd, S. Kobus, N. Manor, S. Alsheikh, D. Duran, L. Bunch, E. Morphis, L. Colasanto, K. H. Hoang, B. Layton, P. Neuhaus, M. Johnson, and J. Pratt, "Summary of team IHMC's virtual robotics challenge entry," in *Proc. 13th IEEE-RAS Int. Conf. Humanoid Robots*, 2013, pp. 307–314.
- [45] R. Tedrake, M. F. Fallon, S. Karumanchi, S. Kuindersma, M. E. Antone, T. Schneider, T. M. Howard, M. R. Walter, H. Dai, R. Deits, M. Fleder, D. Fourie, R. Hammoud, S. Hemachandra, P. Ilardi, C. Perez-D'Arpino, S. Pillai, A. Valenzuela, C. Cantu, C. Dolan, I. Evans, S. Jorgensen, J. Kristeller, J. A. Shah, K. Iagnemma, and S. Teller, "A summary of team MIT's approach to the virtual robotics challenge," in *Proc. IEEE Int. Conf. Robotics and Automation (ICRA)*, 2014, p. 2087. doi: 10.1109/ICRA.2014.6907140.
- [46] E. R. Westervelt, J. W. Grizzle, C. Chevallereau, J. H. Choi, and B. Morris, *Feedback Control of Dynamic Bipedal Robot Locomotion*. Boca Raton, FL: CRC Press, 2007.
- [47] B. Griffin and J. Grizzle, "Walking gait optimization for accommodation of unknown terrain height variations," in *Proc. American Control Conf.*, 2015, pp. 4810–4817.
- [48] K. Galloway, K. Sreenath, A. D. Ames, and J. W. Grizzle, "Torque saturation in bipedal robotic walking through control Lyapunov function based quadratic programs," *IEEE Access*, vol. 3, pp. 323–332, Apr. 2015.
- [49] Q. Nguyen and K. Sreenath, "Optimal robust control for bipedal robots through control Lyapunov function based quadratic programs," in *Proc. Robotics: Science and Systems*, 2015.
- [50] A. Hereid, C. M. Hubicki, E. A. Cousineau, and A. D. Ames, "Dynamic humanoid locomotion: A scalable formulation for HZD gait optimization," *IEEE Trans. Robot.*, vol. 34, no. 2, pp. 370–387, 2018.
- [51] D. Quintero, D. J. Villarreal, D. J. Lambert, S. Kapp, and R. D. Gregg, "Continuous-phase control of a powered knee-ankle prosthesis: Amputee experiments across speeds and inclines," *IEEE Trans. Robot.*, vol. 34, no. 3, pp. 686–701, 2018.
- [52] H. Zhao, J. Horn, J. Reher, V. Paredes, and A. D. Ames, "Multicontact locomotion on transfemoral prostheses via hybrid system models and optimization-based control," *IEEE Trans. Autom. Sci. Eng.*, vol. 13, no. 2, pp. 502–513, 2016.
- [53] A. Agrawal, O. Harib, A. Hereid, S. Finet, M. Masselin, L. Praly, A. D. Ames, K. Sreenath, and J. W. Grizzle, "First steps towards translating HZD control of bipedal robots to decentralized control of exoskeletons," *IEEE Access*, vol. 5, pp. 9919–9934, Apr. 2017.
- [54] T. Gurriet, S. Finet, G. Boeris, A. Hereid, O. Harib, M. Masselin, J. Grizzle, and A. D. Ames, "Towards restoring locomotion for paraplegics: Realizing dynamically stable walking on exoskeletons," in *Proc. 2018 IEEE Int. Conf. Robotics and Automation (ICRA)*, 2018, pp. 2804–2811.
- [55] Y. Hurmuzlu, F. Génot, and B. Brogliato, "Modeling, stability and control of biped robots—A general framework," *Automatica*, vol. 40, no. 10, pp. 1647–1664, 2004.
- [56] J. W. Grizzle, C. Chevallereau, R. W. Sinnet, and A. D. Ames, "Models, feedback control, and open problems of 3-D bipedal robotic walking," *Automatica*, vol. 50, no. 8, pp. 1955–1988, 2014.
- [57] ROS.org. Accessed on: Nov. 4, 2017. [Online]. Available: <http://wiki.ros.org/urdf>
- [58] A. Hereid and A. D. Ames, "Frost: Fast robot optimization and simulation toolkit," in *Proc. IEEE/RSJ Int. Conf. Intelligent Robots and Systems (IROS)*, 2017, pp. 719–726.
- [59] M. Vukobratovic' and B. Borovac, "Zero-moment point—Thirty-five years of its life," *Int. J. Humanoid Robot.*, vol. 1, no. 01, pp. 157–173, 2004.
- [60] A. D. Ames, "Human-inspired control of bipedal walking robots," *IEEE Trans. Autom. Control*, vol. 59, no. 5, pp. 1115–1130, 2014.
- [61] T. Wang and C. Chevallereau, "Stability analysis and time-varying walking control for an under-actuated planar biped robot," *Robot. Auton. Syst.*, vol. 59, no. 6, pp. 444–456, 2011.
- [62] J. Reher, E. A. Cousineau, A. Hereid, C. M. Hubicki, and A. D. Ames, "Realizing dynamic and efficient bipedal locomotion on the humanoid robot durus," in *Proc. IEEE Int. Conf. Robotics and Automation (ICRA)*, 2016, pp. 1794–1801.
- [63] S. Kolathaya, J. Reher, A. Hereid, and A. D. Ames, "Input to state stabilizing control Lyapunov functions for robust bipedal robotic locomotion," in *Proc. American Control Conference (ACC)*, 2018, pp. 2224–2230.
- [64] X. Da and J. Grizzle. (2018). Combining trajectory optimization, supervised machine learning, and model structure for mitigating the curse of dimensionality in the control of bipedal robots. arXiv. [Online]. Available: <https://arxiv.org/abs/1711.02223>
- [65] M. W. Spong, "Partial feedback linearization of underactuated mechanical systems," in *Proc. IEEE/RSJ/GI Int. Conf. Intelligent Robots and Systems. Advanced Robotic Systems and the Real World (IROS)*, 1994, pp. 314–321.
- [66] P. Zaytsev, S. J. Hasaneini, and A. Ruina, "Two steps is enough: No need to plan far ahead for walking balance," in *Proc. IEEE Int. Conf. Robotics and Automation (ICRA)*, 2015, pp. 6295–6300.
- [67] Michigan Robotics: Dynamic Legged Locomotion Lab, "Exoskeleton simulation," YouTube. Accessed on: Sept. 14, 2018. [Online]. Available: https://www.youtube.com/watch?v=7O1-Uly_S8I
- [68] B. Griffin and J. Grizzle, "Nonholonomic virtual constraints and gait optimization for robust walking control," *Int. J. Robot. Res.*, vol. 36, no. 8, pp. 895–922, 2017.